J. Fluid Mech. (2025), *vol.* 1015, A26, doi:10.1017/jfm.2025.10341

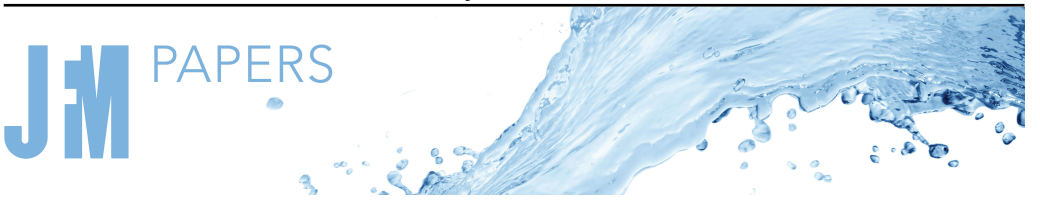

Wave- and potential-driven instabilities in orbital pilot-wave dynamics

Nicholas Liu[1], **Matthew Durey**[2] **and John W.M. Bush**[1]

[1]Department of Mathematics, Massachusetts Institute of Technology, Cambridge, MA 02139, USA

[2]School of Mathematics and Statistics, University of Glasgow, University Place, Glasgow G12 8QQ, UK

Corresponding authors: Matthew Durey, matthew.durey@glasgow.ac.uk; John W. M. Bush, bush@math.mit.edu

(Received 4 December 2024; revised 26 April 2025; accepted 6 June 2025)

We present the results of a theoretical investigation of orbital stability in pilot-wave hydrodynamics, wherein a droplet bounces and self-propels across the surface of a vertically vibrating liquid bath. A critical notion in pilot-wave hydrodynamics is that the bath plays the role of the system memory, recording the history of the droplet in its wave field. Quantised orbital motion may arise when the droplet is confined by either an axisymmetric potential or the Coriolis force induced by system rotation. We here elucidate the dependence of the stability of circular orbits on both the form of the confining force and the system memory. We first provide physical insight by distinguishing between potential- and wave-driven instabilities. We demonstrate that the former are a generic feature of classical orbital dynamics at constant speed, while the latter are peculiar to pilot-wave systems. The wave-driven instabilities are marked by radial perturbations that either grow monotonically or oscillate at an integer multiple of the orbital frequency, in which case they are said to be resonant. Conversely, for potential-driven wobbling, the instability frequency may be resonant or non-resonant according to the form of the applied potential. Asymptotic analysis rationalises the different stability characteristics for linear-spring and Coriolis forces, the two cases that have been explored experimentally. Our results are generalised to consider other potentials of interest in pilot-wave hydrodynamics, and elucidate the distinct roles of wave- and potential-driven instabilities. Our study highlights the limitations of prior heuristic arguments for predicting the onset of orbital instability.

Key words: Faraday waves, drops

1. Introduction

Pilot-wave hydrodynamics (Bush 2015) was initiated by the discovery of Yves Couder and Emmanuel Fort that millimetric droplets may self-propel or 'walk' across the surface of a vibrating liquid bath, propelled by their own wave field (Couder *et al.* 2005). This walking-droplet system has provided the basis for the nascent field of hydrodynamic quantum analogues, which is devoted to exploring the ability of this system to capture features typically associated with the quantum realm (Bush & Oza 2020). The key feature responsible for the emergent quantum-like behaviour is the non-Markovian nature of the droplet dynamics: the bath serves as the memory of the droplet, the extent of which depends on the longevity of the Faraday pilot-wave field as is prescribed by the vibrational acceleration's proximity to the Faraday threshold (Eddi *et al.* 2011). When the walkers are confined by applied forces, the droplets may execute circular orbits (see figure 1), arising through the balance of the inward confining force and the outward inertial force. At high memory, the circular orbits become quantised owing to the dynamical constraint imposed on the droplet by its pilot wave, which serves as an effective self-potential (Fort *et al.* 2010; Oza *et al.* 2014*a*). We here present the results of a theoretical investigation in which we compare the onset of orbital instability and quantisation for pilot-wave hydrodynamics in the presence of a radial force field and in a rotating frame. Doing so allows us to assess the relative importance of the imposed potential and the memory-induced self-potential on the orbital stability.

Fort *et al.* (2010) examined droplets walking in a rotating frame, so subjected to a Coriolis force. At low memory, the droplet executes anticyclonic inertial orbits at its free-walking speed, in which the outward inertial force is balanced by the confining Coriolis force. The orbital radius reflects this balance and differs from that of classical inertial orbits only through the wave-induced added mass of the droplet (Bush, Oza & Moláček 2014; Oza *et al.* 2014*a*). At higher memory, the droplet encounters its own wake, which comprises a circular corrugation on the free surface, centred on the orbital centre (see figure 1*b*). As a consequence, the droplet is restricted to one of a set of circular orbits with quantised radii corresponding approximately to integer multiples of half the Faraday wavelength (Fort *et al.* 2010; Blitstein, Rosales & Sáenz 2024). This radial quantisation may be rationalised in terms of the successive destabilisation of orbits of other radii as the path memory is increased (Fort *et al.* 2010; Harris & Bush 2014; Oza *et al.* 2014*a*). As the orbital radius is increased progressively, the instabilities are marked by either monotonically growing perturbations or resonant wobbles with a wobbling frequency twice the orbital frequency (Oza *et al.* 2014*a*; Liu, Durey & Bush 2023), as depicted in figure 2(*a*,*b*). At the highest memory considered, Harris & Bush (2014) demonstrated that these quantised orbits destabilise into chaotic trajectories marked by intermittent switching between quantised orbits, a feature captured in accompanying theoretical (Oza *et al.* 2014*a*) and numerical (Oza *et al.* 2014*b*) investigations.

Quantised orbital motion may also be induced when the droplet is confined by a central force. This configuration was first explored experimentally by Perrard *et al.* (2014*a*,*b*), who applied a vertical magnetic field with a radial gradient to a droplet filled with ferrofluid, thereby imparting a linear spring force to the droplet. The authors discovered that the droplet has a propensity for orbits that are quantised in both mean radial position and mean angular momentum, which include circles, lemniscates and trefoils (Labousse *et al.* 2014). While the radii of the circular orbits were found to be quantised in a fashion similar to those arising in a rotating frame (Labousse *et al.* 2016; Durey & Milewski 2017), different instabilities set in as the memory was increased. Specifically, all instabilities were found to be wobbles (Tambasco *et al.* 2016), with the wobbling frequency being either close to 2ω (see figure 2*b*), and thus resonant with the orbital frequency, ω, or close to $\sqrt{2}\omega$

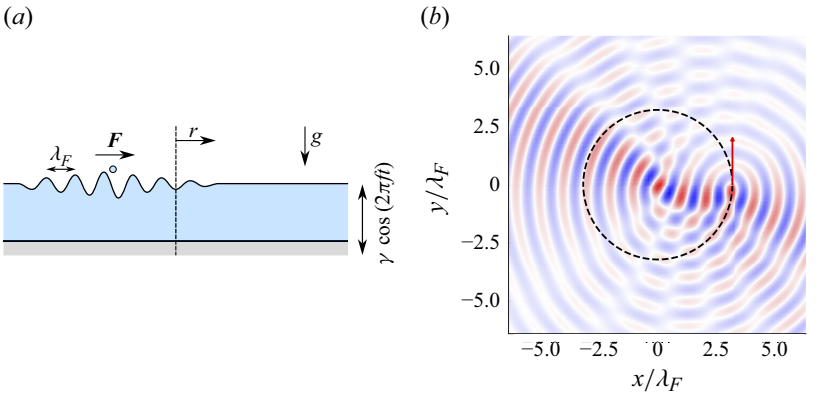

Figure 1. Orbital pilot-wave dynamics in a confining force field. (*a*) Schematic diagram of the physical system, in which a droplet walks along a liquid bath driven vertically with acceleration $\gamma\cos(2\pi ft)$. Two distinct force fields are considered. In the first, the system rotates at an angular velocity $\boldsymbol{\Omega} = \Omega\hat{\boldsymbol{z}}$, so the droplet is subjected to a Coriolis force and is thus prone to anticyclonic circular orbits. In the second, the droplet is constrained by a central force $\boldsymbol{F} = -\boldsymbol{\nabla}V(r)$. The vertical axis represents either the centre of force for a central force, or the rotation axis, $\hat{\boldsymbol{z}}$, in the rotating system. (*b*) Simulated wave field generated by a droplet walking in a circular orbit (black dashed circle) at high memory. Red and blue designate regions of elevation and depression, and white indicates no surface displacement. The Faraday wavelength is $\lambda_F = 4.75$ mm for the experimental parameters detailed in § 3.

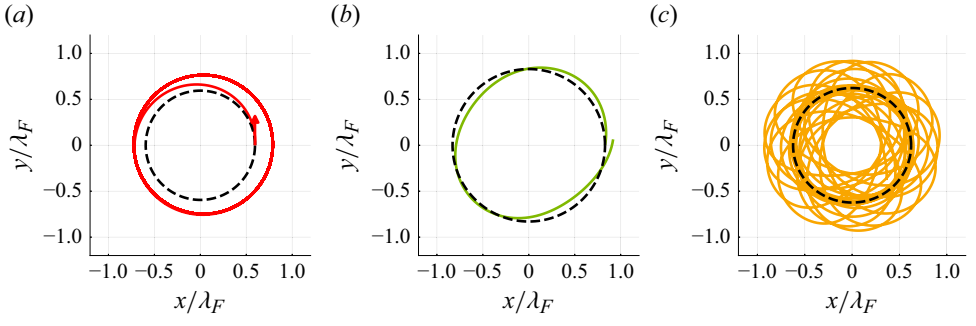

Figure 2. Three forms of orbital instability. Evolution of the droplet trajectory when perturbed from an unstable circular orbit (dashed curve), with (*a*) a monotonic instability, (*b*) a 2ω instability and (*c*) a $\sqrt{2}\omega$ instability, where ω is the orbital frequency. Monotonic instabilities lead to a jump up/down to a nearby stable circular orbit, 2ω-instabilities lead to a stable 2-wobble orbit and $\sqrt{2}\omega$-instabilities lead to quasi-periodic wobbling, for which the wobbling frequency is incommensurate with the orbital frequency. Monotonic and 2ω-instabilities are prevalent for orbital motion in a rotating frame, whereas 2ω- and $\sqrt{2}\omega$-wobbles mark the onset of instability in the presence of a linear spring force.

(see figure 2*c*), and thus non-resonant (Labousse & Perrard 2014). As arose in the rotating frame, at higher memory, the periodic orbital states destabilise, leading to an intermittent switching between unstable periodic orbits (Perrard *et al.* 2014*a*,*b*).

A similar progression from periodic orbits to chaotic trajectories was reported by Cristea-Platon, Sáenz & Bush (2018) in their study of walkers confined to circular corrals. Specifically, as the memory was increased progressively, periodic orbital states, such as circles, lemniscates and trefoils, gave way to chaotic motion marked by intermittent switching between these orbits, a progression also captured in the simulations of Durey, Milewski & Wang (2020*a*). The effective radial force imparted to the droplet by the

submerged topography has been likened to that of a potential that is flat within the corral and increases steeply over the submerged step (Hélias & Labousse 2023), as might be modelled by a power-law radial potential (Cristea-Platon *et al.* 2018). Circular orbits have also been observed for walkers over inverted conical topography, for which an effective radial confining potential of the form $V(r) \propto r$ was inferred for circular orbits (Turton 2020). Orbiting in response to other confining potentials, including a logarithmic (two-dimensional Coulomb) potential (Tambasco *et al.* 2016) and an oscillatory potential of Bessel form (Tambasco & Bush 2018), have been explored numerically. Thus, while walker motion in response to Coriolis and linear central forces will be the focus of our study, we will extend our analysis to consider more general radial forces of interest in pilot-wave hydrodynamics.

Owing to the complexity of orbital pilot-wave dynamics and the associated linear stability analysis, several heuristic arguments have been proposed in an attempt to predict the critical radii of instability. For a linear central force, Labousse *et al.* (2016) noted that the critical radii correspond approximately to zeros of Bessel functions, which was rationalised in terms of the resonance between the perturbation and the system's wave modes. Durey (2018) noted that the orbits with the largest wave energy destabilise at the lowest memory and do so with monotonically growing perturbations. The efficacy of both these heuristic arguments was tested by Liu *et al.* (2023) for orbiting in response to a Coriolis force: although a favourable agreement in the critical radii was obtained, neither heuristic argument accounted for the dependence of the critical radii on droplet inertia. For orbiting in a rotating frame, Liu *et al.* (2023) suggested that one can predict the form of orbital instability of a circular orbit of a given radius according to the form of the local mean pilot wave, which acts as a self-potential at high memory. Specifically, monotonic instabilities were found to arise for orbits where the local mean wave force increases with orbital radius, with wobbling instabilities appearing otherwise. We note, however, that all three heuristic arguments are based solely on the structure of the wave field and so cannot predict either the critical memory or the frequency of instability as they do not take into account the form of the external force field.

We here present a theoretical study of the stability of circular orbits for walkers confined by a radial or Coriolis force, the two systems that have been considered experimentally. When the orbits are unstable, three possibilities exist: monotonically growing perturbations, or wobbling at a frequency that is either resonant or non-resonant with the orbital frequency, as detailed in figure 2. We demonstrate that the frequency of instability depends on the relative influence of the wave-induced self-potential and the applied potential. Wave-driven wobbling, which is peculiar to pilot-wave systems, is always resonant. Potential-driven wobbling, which we show to be a generic feature of classical particle motion at constant speed, may be resonant or non-resonant, depending on the precise form of the confining potential.

In § 2, as a point of comparison for the hydrodynamic pilot-wave system, we consider classical orbital mechanics (specifically, constrained particle motion in the absence of a pilot wave) at constant speed. Doing so reveals the frequency of potential-driven wobbling, but does not yield insight into the influence of memory, specifically the geometric constraint imposed by the pilot-wave field, on orbital stability. This dependence is investigated in § 3 by applying linear stability analysis to the stroboscopic pilot-wave model (Oza, Rosales & Bush 2013) and so constructing numerically the system's orbital stability diagram. We highlight the differences between orbital stability in the Coriolis and linear central force systems as the orbital radius and memory are varied, and classify the emergence of wave- and potential-driven instabilities. In § 4, we use asymptotic analysis to deduce the dependence of the critical memory and frequency of instability on the orbital

radius for both wave-driven and potential-driven instabilities. We then generalise our analysis to consider the stability of orbits in a variety of confining potentials considered in prior studies of pilot-wave hydrodynamics. Particular attention is given to power-law radial force fields, as may play a role analogous to topographic confinement in, for example, the corral experiments (Harris *et al.* 2013; Cristea-Platon *et al.* 2018). In § 5, we discuss the emerging physical picture for orbital stability in pilot-wave hydrodynamics along with potential directions for future research.

2. Physical picture

We first consider the behaviour of particles executing circular orbits in the plane in the presence of an axisymmetric potential. Celestial mechanics, wherein satellites or planets may execute circular orbits under the influence of the gravitational force, provides a valuable point of comparison for our study. In such classical orbital dynamics (in which there is no pilot wave), the form of the applied external potential affects the stability of circular orbits. Specifically, it is well established that stable circular orbits in the plane can only be supported for confining potentials of the form $V(r) \propto r^q$ provided $q > -2$ (Goldstein, Poole & Safko 2002). We begin by re-deriving this result in § 2.1, and then compare it to the analogous stability condition relevant to the hydrodynamic pilot-wave system in § 2.2.

2.1. *Classical orbital mechanics*

We consider the dynamics of a particle of mass m moving in response to an axisymmetric potential, $V(r)$, in two dimensions. By denoting the particle position in polar coordinates as $\boldsymbol{x}_p(t) = r(t)(\cos\theta(t), \sin\theta(t))$, one may express the radial force balance as

$$m(\ddot{r} - r\dot{\theta}^2) = -V'(r). \tag{2.1}$$

Conservation of angular momentum implies that $l = mr^2\dot{\theta}$ is constant for all time. By substituting $\dot{\theta} = l/mr^2$ into (2.1), we deduce that the radial motion of the particle satisfies

$$m\ddot{r} = -V'_{eff}(r), \quad \text{where} \quad V_{eff}(r) = V(r) + \frac{l^2}{2mr^2} \tag{2.2}$$

is the effective potential. Notably, the effective potential is the sum of the applied potential and the so-called centrifugal barrier, which is a potential barrier arising due to the conservation of angular momentum that prevents the particle from approaching the origin.

For steady orbital motion with radius r_0, the radial force balance implies that $l^2 = mr_0^3 V'(r_0)$, which can be satisfied only when $V'(r_0) > 0$. If $r(t) = r_0 + \epsilon r_1(t)$, the radial perturbation will necessarily evolve according the linearised equation $\ddot{r}_1 + \omega_c^2 r_1 = 0$, where

$$\omega_c^2 = \frac{V''_{eff}(r_0)}{m}, \quad \text{or} \quad \omega_c^2 = \omega^2\left(3 + \frac{r_0 V''(r_0)}{V'(r_0)}\right), \tag{2.3}$$

and $\omega = l/mr_0^2$ is the orbital frequency. For a power-law potential of the form $V(r) \propto r^q$, we deduce from (2.3) the relationship $\omega_c^2 = (q+2)\omega^2$, which may be used to assess the linear stability of circular orbits. If $q \leqslant -2$, perturbations grow in time, with circular orbits thus being unstable. Circular orbits thus destabilise if the confining force decays too quickly. Conversely, circular orbits are stable for $q > -2$, with radial perturbations undergoing closed orbits in phase space. Notably, the perturbation frequency, ω_c, is generally incommensurate with the orbital frequency, ω, except when $q+2$ is a perfect square.

2.2. *Orbital mechanics at a constant speed*

A key feature of orbital pilot-wave dynamics in a rotating frame is that the walker speed remains close to the free-walking speed, u_0. While substantial speed variations arise for walker motion in a central force (Perrard *et al.* 2014*b*; Kurianski, Oza & Bush 2017), one expects such variations to be small for nearly circular orbits. To gain insight into the influence of a fixed speed on the stability of circular orbits, we consider the planar motion of a particle of mass m moving in response to a potential, V, with the particle speed fixed at u_0 for all time. The radial motion of the particle is thus governed by (2.1), whereas the constancy of the particle speed gives rise to the condition $u_0^2 = \dot{r}^2 + r^2\dot{\theta}^2$. By eliminating $\dot{\theta}^2$ from (2.1), we deduce that the radial motion of the constant-speed particle is governed by

$$m\left(\ddot{r} + \frac{\dot{r}^2}{r}\right) = -V'_{eff}(r), \quad \text{where} \quad V_{eff}(r) = V(r) - mu_0^2 \ln\left(\frac{r}{r_0}\right) \tag{2.4}$$

is an effective potential, analogous to (2.2) for particle motion in the plane. Notably, the centrifugal barrier for constant-speed dynamics is now logarithmic, which alters the stability of circular orbits relative to those considered in § 2.1.

In a manner similar to § 2.1, we deduce that the steady orbital radius satisfies $mu_0^2 = r_0 V'(r_0)$ for $V'(r_0) > 0$. Furthermore, perturbations of the form $r(t) = r_0 + \epsilon r_1(t)$ evolve according to the linearised equation $\ddot{r}_1 + \omega_p^2 r_1 = 0$, where

$$\omega_p^2 = \frac{V''_{eff}(r_0)}{m}, \quad \text{or} \quad \omega_p^2 = \omega^2\left(1 + \frac{r_0 V''(r_0)}{V'(r_0)}\right), \tag{2.5}$$

and $\omega = u_0/r_0$ is the orbital frequency. Notably, ω_p has a form similar to that of ω_c for classical orbital mechanics (see 2.3). Furthermore, the circular orbit is unstable when $V'(r_0) + r_0 V''(r_0) \leqslant 0$, with perturbations growing monotonically in time, but is stable otherwise. We refer to ω_p as the potential-driven frequency as it reflects the influence of the applied potential on the particle dynamics and is independent of the pilot wave.

We proceed by evaluating the potential-driven frequency, ω_p, for different forms of the confining potential relevant to pilot-wave hydrodynamics. For the power-law potential $V(r) \propto r^q$, it follows directly from (2.5) that $\omega_p = \omega\sqrt{q}$. Consequently, the perturbation frequency is scaled by a factor $\sqrt{q}$ relative to the orbital frequency when $q > 0$, with perturbations instead growing in time when $q \leqslant 0$. For the special case of a linear central force, for which $V(r) \propto r^2$, (2.5) indicates that $\omega_p = \sqrt{2}\omega$, which is precisely equal to the instability frequency reported by Labousse & Perrard (2014) for a droplet executing circular orbits in a harmonic potential (see figure 2*c*). We note that Labousse & Perrard (2014) performed their stability analysis of the Rayleigh oscillator in a frame translating, but not rotating, with the orbiting particle, and so their wobbling frequencies of $(1 \pm \sqrt{2})\omega$ are equivalent to $\pm\sqrt{2}\omega$ in our framework. Finally, (2.5) yields $\omega_p = 0$ for the logarithmic potential $V(r) \propto \ln(r)$, corresponding to a two-dimensional Coulomb force, consistent with the prevalent monotonic instabilities identified by Tambasco *et al.* (2016).

A very different physical picture emerges for a constant-speed particle moving in response to a Coriolis force, $\boldsymbol{F} = -2m\boldsymbol{\Omega} \times \dot{\boldsymbol{x}}_p$, where $\boldsymbol{\Omega} = \Omega\hat{\boldsymbol{z}}$ is the rotation vector, aligned orthogonal to the plane of particle motion (see figure 1*a*). In this case, radial perturbations evolve according to the linearised equation $\ddot{r}_1 + \omega^2 r_1 = 0$, where $\omega = -2\Omega$ is the orbital frequency. The perturbation is neutrally stable, representing a periodic oscillation in the radial distance to the centre of the original orbit at precisely the orbital frequency, ω. This oscillation corresponds to a shift in the orbital centre upon perturbation,

which reflects the fact that the Coriolis force does not depend on the particle position, $\boldsymbol{x}_p$, and is thus invariant to translations. There are thus no potential-driven oscillations for particle motion in a rotating frame.

Our physical picture of walkers as particles moving at a constant speed highlights several features that appear throughout our study. First, the radial perturbation frequency, $\omega_p = \sqrt{q}\omega$, for orbital pilot-wave dynamics differs from that of celestial mechanics, $\omega_c = \sqrt{q+2}\omega$, giving rise to instability in power-law potentials for $q \leqslant 0$ instead of the classical result of $q \leqslant -2$ (Goldstein *et al.* 2002). Second, the potential-driven frequency, ω_p, is exclusive to particle motion confined by a central force, absent for inertial orbits in the rotating frame. Third, the perturbation frequency $\omega_p = \sqrt{q}\omega$ is incommensurate with the orbital frequency, ω, when $\sqrt{q}$ is irrational, but can resonate with the orbital frequency when the potential is such that q is a perfect square. Notably, this simplified physical picture does not account for the influence of memory on orbital pilot-wave dynamics, as expressed through the geometric constraint imposed on the droplet by the quasi-monochromatic pilot-wave field. We thus seek to rationalise the influence of the self-generated wave field on orbital stability for the hydrodynamic pilot-wave system, paying particular attention to evaluating the relative importance of wave-driven and potential-driven instabilities in various settings.

3. Pilot-wave hydrodynamics

We consider the dynamics of a millimetric droplet of mass m, self-propelling across the surface of a liquid bath vibrating vertically with frequency f and acceleration $\gamma\cos(2\pi f t)$; see figure 1(*a*). When the vibrational acceleration exceeds the Faraday threshold, $\gamma > \gamma_F$, the fluid surface is unstable to standing, subharmonic Faraday waves with period $T_F = 2/f$ and wavelength $\lambda_F = 2\pi/k_F$, where k_F is prescribed by the water-wave dispersion relation, $(\pi f)^2 = (gk_F + \sigma k_F^3/\rho)\tanh(k_F\mathcal{H})$ (Benjamin & Ursell 1954). The parameter range of interest is $\gamma < \gamma_F$, corresponding to an undisturbed bath in the absence of the droplet. We focus on the hydrodynamic parameter regime considered by Harris & Bush (2014), who used a silicone oil of density $\rho = 949$ kg m^{-3}, kinematic viscosity $\nu = 20$ cSt and surface tension $\sigma = 0.0206$ N m^{-1}. The bath was $\mathcal{H} = 4$ mm deep and subjected to a vibrational frequency of $f = 80$ Hz. The droplet had radius $R = 0.4$ mm and a free-walking speed of approximately $u_0 = 11$ mm s^{-1}, with an impact phase of $\sin\Phi = 0.2$ (Oza *et al.* 2014*b*). Further parameters are given in table 1.

3.1. *Integro-differential trajectory equation*

The droplet's horizontal motion is modelled using the stroboscopic trajectory equation developed by Oza *et al.* (2013, 2014*a*), as is deduced by time-averaging the dynamics over a bouncing period, T_F (Moláček & Bush 2013). The droplet's horizontal position, $\boldsymbol{x}_p(t)$, thus evolves according to

$$m\ddot{\boldsymbol{x}}_p + D\dot{\boldsymbol{x}}_p = -mg\nabla h(\boldsymbol{x}_p(t), t) + \boldsymbol{F}, \tag{3.1a}$$

where upper dots denote differentiation with respect to time, t. The drop is propelled by the wave force, $-mg\nabla h(\boldsymbol{x}_p, t)$, and resisted by the linear drag force, $-D\dot{\boldsymbol{x}}_p$. We consider two different forms of the external force, $\boldsymbol{F}$ (see figure 1). For a droplet in a rotating frame, the droplet is subjected to a Coriolis force, $\boldsymbol{F} = -2m\boldsymbol{\Omega}\times\dot{\boldsymbol{x}}_p$, where $\boldsymbol{\Omega} = \Omega\hat{\boldsymbol{z}}$ is the vertical rotation vector. When the droplet is confined by an axisymmetric potential, $V(|\boldsymbol{x}|)$, the applied force is $\boldsymbol{F} = -\nabla V(|\boldsymbol{x}_p|)$.

The stroboscopic pilot wave,

$$h(\boldsymbol{x}, t) = \frac{A}{T_F}\int_{-\infty}^{t} \mathrm{J}_0(k_F|\boldsymbol{x} - \boldsymbol{x}_p(s)|)\mathrm{e}^{-(t-s)/T_M}\,\mathrm{d}s, \tag{3.1b}$$

Dimensional parameters	Definition
m, R	Droplet mass, radius
σ, ρ	Liquid surface tension, density
ν, ν_{eff}	(Effective) liquid kinematic viscosity
$\mathcal{H}$, g	Liquid bath depth, gravitational acceleration
μ_{air}, ρ_{air}	Air dynamic viscosity, density
f, γ	Vibrational forcing frequency, acceleration
γ_F	Faraday instability threshold
λ_F, $k_F = 2\pi/\lambda_F$, $T_F = 2/f$	Faraday wavelength, wavenumber, period
$T_d = (\nu_{eff} k_F^2)^{-1}$	Wave decay time in the absence of forcing
$T_M = T_d/(1-\gamma/\gamma_F)$	Wave decay (memory) time
Φ	Mean phase of wave during contact
$A = \sqrt{\frac{\nu_{eff} T_F}{2\pi}} \frac{mgk_F^3 \sin\Phi}{3k_F^2\sigma + \rho g}$	Amplitude of single surface wave
$D = 0.17mg\sqrt{\frac{\rho R}{\sigma}} + 6\pi\mu_{air} R\left(1 + \frac{\rho_{air} g R}{12\mu_{air} f}\right)$	Drag coefficient
$F = mgAk_F$	Wave force coefficient
$c = \sqrt{F/DT_F k_F}$	Maximum walking speed
$T_W = \sqrt{2}/ck_F$, $\gamma_W/\gamma_F = 1 - T_d/T_W$	Memory time (vibrational acceleration) at walking threshold
$u_0 = (c/2)\sqrt{4 - (1-\Gamma)^2 - (1-\Gamma)\sqrt{(1-\Gamma)^2+8}}$	Free-walking speed
$\boldsymbol{\Omega}$, k	Rotation vector, spring constant
r_0, ω, $U = r_0\omega$	Orbital radius, angular frequency, speed
$T_O = 2\pi/\omega$	Orbital period
s	Asymptotic complex growth rate of perturbations
$S = \lvert\mathrm{Im}(s)\rvert$	Perturbation frequency

Dimensionless parameters	Definition
$M = mck_F/D$	Inertia-to-drag ratio
$\Gamma = (\gamma - \gamma_W)/(\gamma_F - \gamma_W)$	Memory parameter
$\hat{r}_0 = r_0 k_F$, $\hat{\omega} = \omega/ck_F$, $\hat{U} = \hat{r}_0\hat{\omega}$	Dimensionless orbital radius, angular frequency, speed
$M_e^O = T_M/T_O$	Orbital memory
$\beta = 1/\omega T_M = 1/2\pi M_e^O$	Reciprocal orbital memory parameter
$\hat{s} = s/ck_F$	Dimensionless complex growth rate
$\xi = S/\omega$	Wobble number

Table 1. Parameters appearing in the pilot-wave system (3.2) and subsequent analysis.

is modelled as a continuous superposition of axisymmetric waves of amplitude A centred along the droplet's path, decaying exponentially in time over the memory time scale, $T_M = T_d/(1-\gamma/\gamma_F)$, where T_d is the viscous decay time of the waves in the absence of vibrational forcing (Oza *et al.* 2013). The slower the waves decay, the greater the influence of the waves generated along the droplet's path and so the longer the droplet's path memory. Projecting the pilot wave onto the droplet's path makes clear the influence of path memory on the droplet motion, as is encapsulated within the integro-differential trajectory equation (Oza *et al.* 2013, 2014*a*)

$$m\ddot{\boldsymbol{x}}_p + D\dot{\boldsymbol{x}}_p = \frac{F}{T_F}\int_{-\infty}^{t} \frac{\mathrm{J}_1(k_F|\boldsymbol{x}_p(t) - \boldsymbol{x}_p(s)|)}{|\boldsymbol{x}_p(t) - \boldsymbol{x}_p(s)|}(\boldsymbol{x}_p(t) - \boldsymbol{x}_p(s))\mathrm{e}^{-(t-s)/T_M}\,\mathrm{d}s + \boldsymbol{F}, \quad (3.2)$$

where $F = mgAk_F$ denotes the magnitude of the wave force. The quasi-monochromatic form of the pilot-wave field imposes a geometric constraint on the droplet's motion whose effects are most pronounced at high memory, where the Faraday waves are most persistent.

Although the stroboscopic model (3.1) has adequately captured the majority of walker behaviours, it is based on the assumption that the droplet bounces in perfect resonance with the oscillation of the Faraday wave field. Recent work has demonstrated that significant non-resonant effects arise when droplets navigate a substantial wave field (Primkulov *et al.* 2025*a*,*b*); their role in orbital stability will be considered elsewhere. We also neglect the exponential far-field decay of the wave field (Tadrist *et al.* 2018; Turton, Couchman & Bush 2018), which one expects to influence the stability of large circular orbits. Finally, we focus on small-amplitude perturbations from circular orbits; thus, our linear theory cannot lend insight into nonlinear effects as are responsible for the emergence of trefoil and lemniscate trajectories in a central force (Perrard *et al.* 2014*a*,*b*).

3.2. *Memory and orbital memory*

In the absence of an applied force, the droplet self-propels at a constant speed, $u_0(\gamma)$, when the vibrational acceleration, γ, exceeds the walking threshold, γ_W. As the vibrational forcing remains below the Faraday threshold in experiments, $\gamma < \gamma_F$, it is convenient to characterise the pilot-wave dynamics in terms of the dimensionless memory parameter $\Gamma = (\gamma - \gamma_W)/(\gamma_F - \gamma_W)$ (Bush 2015; Oza, Rosales & Bush 2018). Notably, $\Gamma = 0$ corresponds to the walking threshold in the absence of an applied force ($\gamma = \gamma_W$), while $\Gamma = 1$ corresponds to the Faraday threshold ($\gamma = \gamma_F$), and thus infinite path memory. In addition, Γ is related to the wave decay time, T_M, via $\Gamma = 1 - T_W/T_M$, where T_W is the memory time at the walking threshold, γ_W (Durey *et al.* 2020*b*).

For orbital pilot-wave dynamics, a key concept is that of 'orbital memory' (Oza *et al.* 2014*a*), which determines the extent to which an orbiting droplet interacts with its own wake, specifically the waves generated on its prior orbit. The longer the orbital memory, the more pronounced the self-potential. For a droplet moving in a circular orbit at angular frequency ω, the waves generated along the droplet path decay by a factor e^{-T_O/T_M} over the orbital period, $T_O = 2\pi/\omega$. We thus define $M_e^O = T_M/T_O$ as the orbital memory. When the droplet orbits close to its free-walking speed, $u_0 \approx r_0\omega$, the orbital memory, $M_e^O \approx T_M u_0/(2\pi r_0)$, increases with vibrational forcing and decreases for larger orbits. For $M_e^O \ll 1$, the wave decays quickly relative to the orbital period, so the droplet is largely unperturbed by its wake (see Appendix A). Conversely, if $M_e^O \gg 1$, the droplet is strongly influenced by its past history, with the quasi-monochromatic form of the Faraday wave field imposing a geometric constraint on the droplet motion. The onset of orbital instability arises at an intermediate regime, $M_e^O \approx 1$ (Oza *et al.* 2014*a*). The precise dependence of this critical orbital memory on the orbital radius will be established in § 4.

3.3. *Orbital stability diagram*

We begin by comparing the dynamics of circular orbits for the cases of a droplet propelling subject to a Coriolis force or confined by a linear spring force, $\boldsymbol{F} = -k\boldsymbol{x}_p$. By substituting $\boldsymbol{x}_p(t) = r_0(\cos\omega t, \sin\omega t)$ into (3.2), we deduce the radial and tangential force balances

$$-mr_0\omega^2 = \frac{F}{T_F}\int_0^\infty \mathrm{J}_1\left(2k_F r_0 \sin\left(\frac{\omega s}{2}\right)\right)\sin\left(\frac{\omega s}{2}\right)\mathrm{e}^{-s/T_M}\,\mathrm{d}s + \boldsymbol{F}\cdot\boldsymbol{n}, \tag{3.3a}$$

$$Dr_0\omega = \frac{F}{T_F}\int_0^\infty \mathrm{J}_1\left(2k_F r_0 \sin\left(\frac{\omega s}{2}\right)\right)\cos\left(\frac{\omega s}{2}\right)\mathrm{e}^{-s/T_M}\,\mathrm{d}s + \boldsymbol{F}\cdot\boldsymbol{t}. \tag{3.3b}$$

Notably, the applied tangential force vanishes for droplet motion under the influence of either a Coriolis or a spring force, namely $\boldsymbol{F}\cdot\boldsymbol{t}=0$. Furthermore, $\boldsymbol{F}\cdot\boldsymbol{n}=2m\Omega r_0\omega$ for a Coriolis force and $\boldsymbol{F}\cdot\boldsymbol{n}=-kr_0$ for the linear spring force. We consider counter-clockwise orbital motion with $\omega>0$, so that $U=r_0\omega$ is the orbital speed. Owing to the droplet's tendency to move along circular orbits at speeds close to the free-walking speed, u_0 (Bush *et al.* 2014), the orbital speed satisfies $U\approx u_0$ and is bounded above by the maximum steady walking speed, specifically that arising at the Faraday threshold, $c=u_0(\gamma_F)$ (Liu *et al.* 2023).

In figure 3, we present the stability of circular orbits for a droplet moving in response to a Coriolis force or a linear spring force (the details of which are outlined in Appendices B and C). The orbital dynamics is parametrised by the memory parameter, Γ, and the orbital radius, r_0, which together determine the form of the Faraday wave field, or self-potential (Oza *et al.* 2014*a*, 2018). The path memory endows the system with infinitely many eigenvalues. The stability of each orbit is thus characterised by the eigenvalue with largest real part (Oza *et al.* 2014*a*), denoted s_*, with the perturbation growing when $\mathrm{Re}(s_*)>0$ and oscillating when $\mathrm{Im}(s_*)\neq 0$. At low memory, all orbits are found to be stable, as detailed in Appendix A (Oza 2014). As the memory parameter is increased, stable circular orbits (blue) destabilise progressively via either monotonically growing (red) or wobbling (green or orange) instability mechanisms. Stable circular orbits are thus quantised in radius at high memory, corresponding to the blue plateaus in figure 3(*a*,*b*). We summarise the orbital stability for all values of Γ in the stability diagram (figure 3*c*,*d*), where instabilities appear as 'tongues' separating intervals of quantised stable radii.

We characterise the dependence of the instability mechanism on the orbital radius in terms of the wobble number, $\xi=S/\omega$, defined as the ratio of the instability frequency, $S=|\mathrm{Im}(s_*)|$, to the orbital frequency, ω. The wobble number on the stability boundary (denoted by the white curve in figure 3*c*,*d*) varies significantly with the orbital radius, as is evident from the grey curves in figure 3(*e*,*f*). Discontinuities in ξ correspond to changes in the instability mechanism. Specifically, ξ switches between intervals of monotonic instabilities ($\xi=0$) and wobbling instabilities ($\xi>0$) as r_0 increases over a length scale comparable to half the Faraday wavelength. As is summarised in table 2, the instability mechanism alternates between monotonic instabilities and 2-wobbles for a Coriolis force (Oza *et al.* 2014*a*,*b*). For a linear spring force, monotonic instabilities are subdominant to wobbling instabilities at frequencies 2ω (green) and $\omega_p=\sqrt{2}\omega$ (orange; see § 2.2), corresponding to resonant wave-driven 2-wobbles (Harris & Bush 2014) and non-resonant potential-driven wobbling, respectively.

Despite the complexity of the orbital stability problem, monotonic instabilities have a particularly simple form. Specifically, circular orbits have an unstable real eigenvalue (corresponding to monotonic growth) in the upward-sloping portions of the orbital solution curves in figure 3(*a*,*b*); see Theorem 1 of Oza *et al.* (2014*a*) for a proof in the case of a Coriolis force and Theorem 1 (Appendix B) for a generalised proof applicable to both Coriolis and central forces. For a Coriolis force, these monotonic instabilities are responsible for the onset of orbital quantisation. For a linear spring force, however, monotonic instabilities are subdominant to potential-driven wobbling, which instead drive the onset of orbital quantisation.

Two further instabilities, common to both the Coriolis force and the linear spring force, are evident in figure 3. First, we note that the wobble number, ξ, approaches 3 when r_0/λ_F is just below a half-integer multiple of the Faraday wavelength for small orbits (see figure 3*e*,*f*). This instability corresponds to the 3-wobbles identified in the numerical simulations of Oza *et al.* (2014*b*) within small portions of parameter space, but they have proven to be elusive in the laboratory (Harris & Bush 2014). Second, we note that large

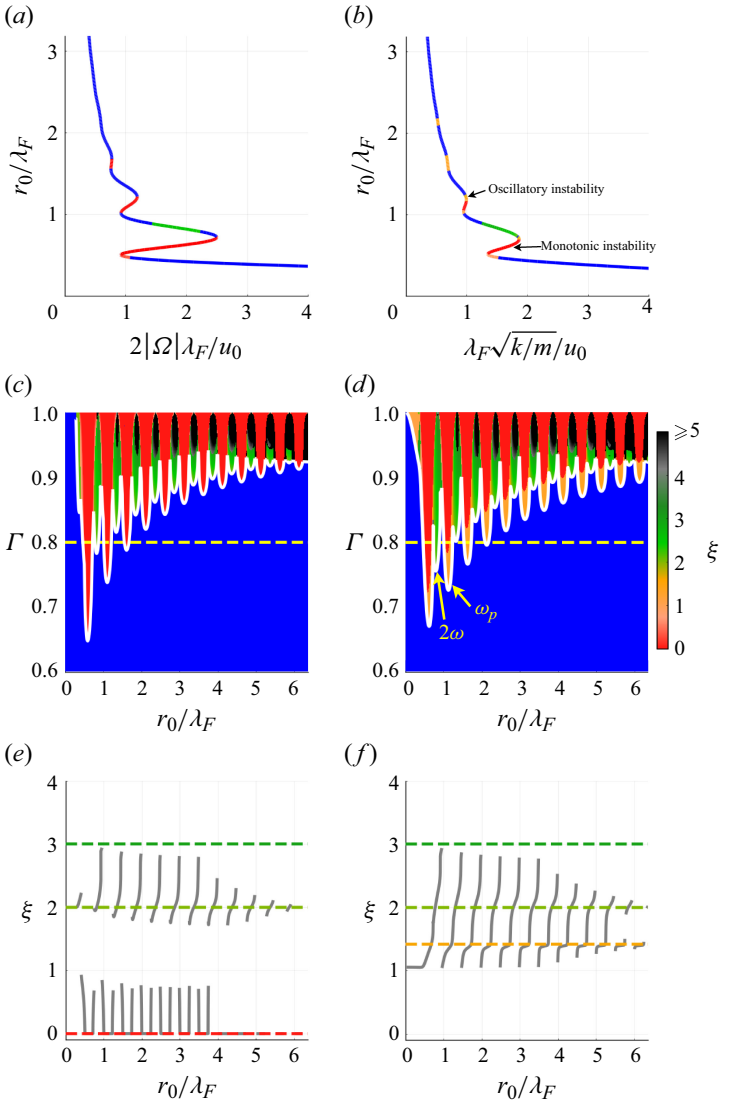

Figure 3. Stability of circular orbits for (*a*,*c*,*e*) a Coriolis force and (*b*,*d*,*f*) a linear spring force. (*a*,*b*) Relationship between the orbital radius, r_0, and (*a*) the rotation rate, Ω, or (*b*) the spring constant, k, for circular orbits with memory parameter $\Gamma = 0.8$. Blue portions of the curve denote stable circular orbits, with red, green and orange indicating unstable orbits, colour-coded by the corresponding wobble number, $\xi = S/\omega$. (*c*,*d*) Orbital stability diagram for a range of Γ, with the yellow dashed line corresponding to the orbital curve in panels (*a*,*b*). The white curve denotes the stability boundary, above which all circular orbits are unstable. Quantised orbits emerge between the instability tongues. We note the additional orange regions in panel (*d*), corresponding to $\omega_p = \sqrt{2}\omega$ instabilities. (*e*,*f*) Dependence of the wobble number, ξ (grey curve), along the stability boundary (white curve in panels *c*,*d*). Discontinuities in ξ correspond to changes in the instability mechanism. The dashed lines correspond to $\xi = 0$, $\xi = \sqrt{2}$, $\xi = 2$ and $\xi = 3$. Monotonic instabilities are subdominant to potential-driven instabilities for a linear spring force and so are not evident in panel (*f*).

values of the wobble number ($\xi \geqslant 5$) are evident in the black portions of figure 3(*c*,*d*), appearing only at high memory. This instability corresponds to speed oscillations over a length scale comparable to the Faraday wavelength (Bacot *et al.* 2019; Hubert *et al.* 2019; Durey *et al.* 2020*b*), for which $\xi \approx r_0 k_F$ (Liu *et al.* 2023). For orbits larger than

	$\sin(2k_F r_0) > 0$	$\sin(2k_F r_0) < 0$
Coriolis force	Monotonic instability	2ω-instability
Linear spring force	ω_p-instability (Monotonic instability)	2ω-instability

Table 2. Correspondence between the sign of $\sin(2k_F r_0)$ and the existence of monotonic or wobbling instabilities (at frequency 2ω or $\omega_p = \sqrt{2}\omega$) for orbital motion with radius r_0 and frequency ω subjected to a Coriolis force or a linear spring force. Subdominant instabilities are denoted in parentheses. These results are deduced from the asymptotic analysis in § 4.

those presented in figure 3 (i.e. for $r_0/\lambda_F > 6$), these speed oscillations form the dominant instability mechanism, in accordance with the instability of rectilinear walkers (Durey *et al.* 2020*b*). Owing to the relative scarcity of both 3-wobbles and speed oscillations in the laboratory, we henceforth focus our investigation on monotonically growing perturbations and wave- and potential-driven wobbling.

4. Onset of instability

We proceed to develop asymptotic formulae for the critical memory and frequency of instability for large circular orbits, which we use to explain the structural differences in the stability diagram for different external forces. Motivated by the effective radial force fields inferred for droplet–topography interactions and by the differences in the orbital stability diagram enumerated in § 3.3, we broaden our analysis to encompass the cases of a Coriolis force, $\boldsymbol{F} = -2m\boldsymbol{\Omega} \times \dot{\boldsymbol{x}}_p$, and a power-law central force of the form $\boldsymbol{F} = -k|\boldsymbol{x}_p|^{n-1}\boldsymbol{x}_p$, where k is the spring constant. Notably, the central force may be derived from a power-law potential of the form $V(r) \propto r^{n+1}$ when $n > -1$, and from a logarithmic potential, $V(r) \propto \ln(r)$, when $n = -1$. We pay particular attention to the case of $n+1$ being a perfect square, for which potential-driven wobbling with frequency $\omega_p = \omega\sqrt{n+1}$ resonates with the orbital frequency, leading to a stability diagram of more complex structure. As most circular orbits are found to be unstable with monotonically growing perturbations for $n < -1$ (in accordance with ω_p being imaginary), we consider $n \geqslant -1$ henceforth. We also restrict our attention to $n \leqslant 4$ for the sake of brevity.

To investigate the onset of orbital instability, we leverage linear stability analysis to determine the response of the droplet trajectory when perturbed from a circular orbit following an impulsive force. The linear stability framework is outlined in Appendices B and C, and is derived by taking Laplace transforms of the linearised droplet trajectory equation. The poles of the resultant transfer function correspond to the long-time asymptotic growth rates, s (Oza *et al.* 2014*a*). A key feature of our framework is that the radial force balance (3.3*a*) is used to eliminate the applied force as a parameter in the stability problem. Instead, orbits are parametrised by their radius (Oza 2014; Oza *et al.* 2014*a*; Liu *et al.* 2023), with the corresponding orbital frequency deduced from the tangential force balance (3.3*b*).

4.1. *Asymptotic framework*

We here develop an asymptotic framework for analysing the stability of large circular orbits, for which $r_0 k_F \gg 1$, building upon the analysis of Liu *et al.* (2023) for orbiting in a rotating frame. In so doing, we determine asymptotic formulae for the critical vibrational acceleration along the stability boundary and the corresponding instability frequency, S.

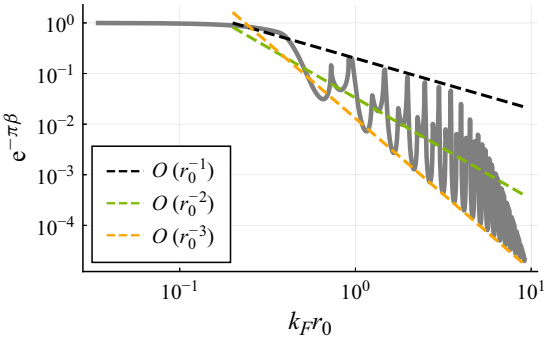

Figure 4. Dependence of the wave damping factor over half an orbital period, denoted $e^{-\pi\beta} = e^{-T_O/(2T_M)}$, at the onset of instability on the orbital radius, r_0, for a linear central force, $\boldsymbol{F} = -k\boldsymbol{x}_p$ ($n = 1$). The grey curve is a rescaling of the stability boundary (white curve) presented in figure 3(*d*). Notably, the envelopes of the instability tongues satisfy the scaling $e^{-\pi\beta} = O(\hat{r}_0^{-l})$ for $l = 2$ and $l = 3$, which are used in the asymptotic analysis presented in § 4.1. The scaling $e^{-\pi\beta} = O(\hat{r}_0^{-1})$ emerges between pairs of instability tongues, including for 3-wobbles, but is outside the scope of this investigation.

These formulae may then be used to compare the relative vibrational forcing at which instabilities occur, as well as the corresponding orbital radii at the tip of each instability tongue. One key inference made from our analysis is the peculiar switching in the structure of the stability boundaries as the force power, n, is varied. This switching demonstrates limitations in prior heuristic arguments for predicting the critical radii of instability tongues solely in terms of zeros of Bessel functions (Labousse *et al.* 2016), the wave energy (Durey 2018) or the structure of the mean wave field (Liu *et al.* 2023).

Central to our analysis is determining suitable scaling relationships between the dimensionless radius, $\hat{r}_0 = k_F r_0 \gg 1$, the dimensionless orbital speed, $\hat{U} = U/c$, the wobble number, $\xi = S/\omega$, and the reciprocal orbital memory parameter, $\beta = 1/(\omega T_M)$, which may be equivalently defined as $\beta = 1/(2\pi M_e^O)$. We recall that $U < c$ for all orbits, with U generally quite close to c at high memory, and so assume that $\hat{U} = O(1)$. Furthermore, as we are investigating monotonic and wobbling instabilities, we assume that $\xi = O(1)$, with the leading-order contribution (and thus wobble number) arising naturally from our analysis. Furthermore, we observe from figure 4 that the wave damping factor over half an orbital period, $e^{-\pi\beta} = e^{-T_O/2T_M}$, scales algebraically with radius along the stability boundary for a linear spring force. Specifically, 2ω-instabilities (green line) satisfy the scaling $e^{-\pi\beta} = O(\hat{r}_0^{-2})$ and ω_p-instabilities (orange line) satisfy $e^{-\pi\beta} = O(\hat{r}_0^{-3})$. The scaling relationship $e^{-\pi\beta} = O(\hat{r}_0^{-2})$ also arises for monotonic and 2ω-instabilities in a Coriolis force (Liu *et al.* 2023), and we find that similar scaling relationships emerge for nonlinear springs. To account for all of these cases, we assume that the dominant balance $\beta = O(\ln \hat{r}_0)$ holds for $\hat{r}_0 \gg 1$, with the particular scaling power $e^{-\pi\beta} = O(\hat{r}_0^{-l})$ being deduced as part of the solution process detailed in Appendix D. We summarise the results of this analysis as follows.

4.2. *Walking in a rotating frame*

Liu *et al.* (2023) demonstrated that orbiting in a Coriolis force gives rise to monotonic and 2ω-instabilities as the vibrational forcing is increased. In terms of the dimensionless mass, $M = mck_F/D$, and reciprocal orbital memory parameter, β, the leading-order approximation for the stability boundary corresponding to monotonic instabilities is

$$\beta_0 = \frac{1}{\pi}\ln\left(\frac{8k_F^2 r_0^2\sin(2k_F r_0)}{1+2M}\right) + O\left(\frac{\ln(k_F r_0)}{k_F r_0}\right), \tag{4.1a}$$

which is valid when $\sin(2k_F r_0) \approx 1$. Notably, maxima in β correspond to minima in Γ (where $\Gamma = 1 - \sqrt{2}\omega\beta/ck_F$ along stability boundaries), which represent the tips of the instability tongues in figure 3(*c*). Similarly, the stability boundary corresponding to 2ω-instabilities is

$$\beta_{2\omega} = \frac{1}{\pi}\ln\left(-\frac{8k_F^2 r_0^2\sin(2k_F r_0)}{3(1+2M)}\right) + O\left(\frac{\ln(k_F r_0)}{k_F r_0}\right), \tag{4.1b}$$

valid when $\sin(2k_F r_0) \approx -1$, where the corresponding wobble number along the stability boundary is

$$\xi_{2\omega} = 2 - \frac{4\beta_{2\omega}}{\pi k_F r_0}\cot(2k_F r_0) + O\left(\frac{1}{k_F^2 r_0^2}\right). \tag{4.1c}$$

The monotonic and 2-wobble instabilities are thus interlaced, with the corresponding instability tongues in figure 3(*c*) alternating over half the Faraday wavelength as the orbital radius is increased. As the critical radii, which lie at the tip of each instability tongue, approximately satisfy $\cos(2k_F r_0) = 0$ for large orbits, the $O(1/k_F r_0)$ correction to $\xi_{2\omega}$ vanishes at the tip of each instability tongue, giving rise to $\xi = 2 + O(1/k_F^2 r_0^2)$. We note also that increasing the dimensionless mass, M, increases the critical memory of instability, corresponding to shortening of the instability tongues in the stability diagram.

4.3. *Walking in a power-law central force*

For orbital motion in a power-law central force, $\boldsymbol{F} = -k|\boldsymbol{x}_p|^{n-1}\boldsymbol{x}_p$, corresponding to $V(r) \propto r^{n+1}$ for $n > -1$, the onset of instability is more intricate, with a subtle dependence of the instability mechanism on the force power, n (see Appendix D). We detail the onset of wave- and potential-driven instabilities as follows.

4.3.1. *Wave-driven instabilities*

For wave-driven resonant instabilities, the wobble number is $\xi \approx 2N$ for any integer $N \geqslant 0$, with $N = 0$ for monotonic instabilities and $N = 1$ for 2-wobbles. The reciprocal orbital memory parameter along the stability boundary (corresponding to $\Gamma = 1 - \sqrt{2}\omega\beta/ck_F$) is

$$\beta_{2N\omega} = \frac{1}{\pi}\ln\left(-\frac{8k_F^2 r_0^2\sin(2k_F r_0)}{(4N^2-n-1)(1+2M)}\right) + O\left(\frac{\ln(k_F r_0)}{k_F r_0}\right), \tag{4.2a}$$

which is valid provided that $|\sin(2k_F r_0)| = O(1)$ and the argument of the logarithm is positive. The corresponding wobble number along the stability boundary is

$$\xi_{2N\omega} = 2N + \frac{N}{\pi k_F r_0}\left(\frac{4M-1}{4N^2-n-1} - 4\beta_{2N\omega}\cot(2k_F r_0)\right) + O\left(\frac{1}{k_F^2 r_0^2}\right), \tag{4.2b}$$

where $\xi_0 = 0$ for monotonic instabilities.

There are two notable similarities in the onset of wave-driven instabilities for the Coriolis and power-law central forces. First, both systems satisfy the asymptotic scaling $\mathrm{e}^{-\pi\beta} = O(\hat{r}_0^{-2})$. Second, wobbling instabilities with $N > 1$ are subdominant to monotonic ($N = 0$) and 2ω ($N = 1$) instabilities in both systems for all $M > 0$, as was shown by

Force power, n	$\sin(2k_F r_0) > 0$	$\sin(2k_F r_0) < 0$
$-1 < n < 0$	Monotonic instability (2ω-instability)	ω_p-instability
$0 < n < 3$	ω_p-instability (Monotonic instability)	2ω-instability
$3 < n \leqslant 4$	2ω-instability (Monotonic instability)	ω_p-instability

Table 3. Correspondence between the sign of $\sin(2k_F r_0)$ and the existence of monotonic and wobbling instabilities (at frequency 2ω or $\omega_p = \omega\sqrt{n+1}$) for a droplet walking in a power-law central force, $\boldsymbol{F} = -k|\boldsymbol{x}_p|^{n-1}\boldsymbol{x}_p$. These results may be deduced by requiring the argument of the corresponding logarithm in (4.2*a*) or (4.4*a*) to be positive. Subdominant instabilities are indicated in parentheses. We restrict our attention to $-1 < n \leqslant 4$ and to the parameters accessible in experiments (for which the dimensionless mass satisfies $4M > 1$).

Liu *et al.* (2023) for a Coriolis force. For a central force, this result may be verified by using (4.2*a*) to deduce that the leading-order stability envelope is defined as

$$\beta_{2N\omega}^{env} = \frac{1}{\pi}\ln\left(\frac{8k_F^2 r_0^2}{|4N^2 - n - 1|(1+2M)}\right), \tag{4.3}$$

which is found by substituting $|\sin(2k_F r_0)| = 1$ into (4.2*a*). The critical memory of instability is thus lower for smaller values of $|4N^2 - n - 1|$, with the two smallest values achieved for $N = 0$ and $N = 1$ for the range of force powers ($-1 < n \leqslant 4$) considered here.

Two important differences in the onset of wave-driven instabilities between the two systems are also apparent. First, the factor of $4N^2 - n - 1$ in (4.2*a*) changes sign for larger n, causing 2ω-instabilities to overlap with monotonic instabilities in the stability diagram for a central force with $n > 3$ (see table 3 and § 4.3.4). Second, the additional $O(1/k_F r_0)$ frequency detuning term in (4.2*b*) leads to an appreciable departure from an exact 2-wobble at the onset of instability relative to a Coriolis force (see 4.1*c*), as was evident in the simulations of Tambasco *et al.* (2016, figure 7*a*) close the stability boundary.

4.3.2. *Potential-driven instabilities*

The stability boundary corresponding to potential-driven wobbling involves the distinct scaling of $\mathrm{e}^{-\pi\beta} = O(\hat{r}_0^{-3})$ (see Appendix D), with

$$\beta_{\omega_p} = \frac{1}{\pi}\log\left(-\frac{16k_F^3 r_0^3 \sin(2k_F r_0)\sin(\pi\xi_{\omega_p})}{\xi_{\omega_p}(4M-1)(2M+1)}\right) \tag{4.4a}$$

along the stability boundary to leading order. As our analysis is focused on the parameter regime accessible in the laboratory (Harris & Bush 2014), for which $M \approx 2.27$, we henceforth restrict our attention to the case $4M > 1$. Consequently, (4.4*a*) is valid provided that (i) $|\sin(2k_F r_0)| \approx 1$ and (ii) $\sin(2k_F r_0)$ and $\sin(\pi\xi_{\omega_p})$ are of opposite signs. Finally,

$$\xi_{\omega_p} = \sqrt{n+1} + o(1) \tag{4.4b}$$

is the leading-order instability frequency, which corresponds precisely to the perturbation frequency $\omega_p = \omega\sqrt{n+1}$ deduced in § 2. As we require $\sin(\pi\xi_{\omega_p}) \neq 0$ in (4.4*a*), our analysis is valid only when ξ_{ω_p} is not an integer (and so $n+1$ cannot be a perfect square), corresponding to non-resonant potential-driven instabilities.

For both wave- and potential-driven instabilities, the critical radii (which maximise β, or minimise Γ, along the stability boundary) satisfy $\sin(2k_F r_0) \approx \pm 1$, with the sign chosen so that the argument of the corresponding logarithm in (4.2*a*) or (4.4*a*) is positive. We summarise the necessary signs of $\sin(2k_F r_0)$ in table 3 as the central force power, $n > -1$, is varied, from which one may rationalise the interlacing and overlapping of the different instability tongues in the stability diagram. Of particular note are (i) the switching in the critical radii of instability between 2ω- and ω_p-instabilities as n exceeds 3 and (ii) the subdominance of monotonic instabilities to wobbling for $n > 0$.

We proceed by outlining the dependence of the stability diagram on the force power, n. We first use our asymptotic results to explain the differences identified in § 3.3 between the stability diagrams for a linear spring force and a Coriolis force (§ 4.3.3). Generalising to consider any convex power-law potential makes clear that one cannot predict the onset of ω_p- and 2ω-instabilities using heuristic arguments based only on the form of the wave field (§ 4.3.4). In § 4.3.5, we detail a new correspondence between the orbital stability diagrams for a conical potential and a Coriolis force. Finally, we characterise the preponderance of monotonic instabilities for concave potentials in § 4.3.6, paying particular attention to the emergence of anomalous instabilities in a logarithmic potential (Tambasco *et al.* 2016).

4.3.3. *Linear central force*

The most notable difference between the stability diagrams for the linear central force ($n = 1$) and the Coriolis force (see figure 3) is the presence of the potential-driven instabilities at frequency $\omega_p = \sqrt{2}\omega$ in the former setting. As predicted by our asymptotic analysis, the ω_p-wobbles form the initial instability mechanism when $\sin(2k_F r_0) > 0$ (see table 3), yet are surpassed by monotonic instabilities as memory is progressively increased (see figure 3*d*). A second difference in the two stability diagrams appears in the envelopes of the monotonic and 2ω-instability tongues: monotonic instabilities emerge at a lower memory than 2ω instabilities in a Coriolis force (Liu *et al.* 2023), whereas the two asymptotic envelopes are identical for a linear spring force (see (4.3) for $n = 1$). This coincidence of monotonic and 2ω stability envelopes for a linear spring force is evident in figure 3 and the stability diagram of Tambasco *et al.* (2016, figure 5), but is not the case for that of Labousse *et al.* (2016, figure 3).

4.3.4. *Convex potentials*

For convex power-law potentials of the form $V(r) \propto r^{n+1}$ with $n > 0$, of which the linear spring force ($n = 1$) is a special case, 2ω- and ω_p-wobbling instabilities are prevalent, as is evident in figure 5 and table 3. The structural reconfiguration in the orbital stability diagram as n exceeds 3 reflects an interchange in the critical radii of instability for 2ω- and ω_p-wobbles. This interchange cannot be predicted by heuristic arguments based solely on consideration of the wave field, specifically the wave energy, zeros of Bessel functions (Labousse *et al.* 2016) or the mean wave field (Liu *et al.* 2023). Although the switch in instability mechanism at $n = 3$ is predicted to be discrete in our asymptotic analysis (see table 3), the transition is continuous in the numerical results. Specifically, the instability tongues merge into a pair at $n = 3$ (for which $\omega_p = 2\omega$) with the wobble number, ξ, being close to 2 along the stability boundary (see figure 5*d–f*). Finally, we note that our asymptotic theory is not valid for $n = 3$ as the condition $\sin(\pi\sqrt{n+1}) \neq 0$ is violated, and thus a special asymptotic treatment would be required in this case.

4.3.5. *Conical potential*

For a conical potential of the form $V(r) \propto r$ (corresponding to $n = 0$), the attractive radial force is independent of radial position, namely $\boldsymbol{F} \cdot \boldsymbol{n} = -k$. This situation is thus similar

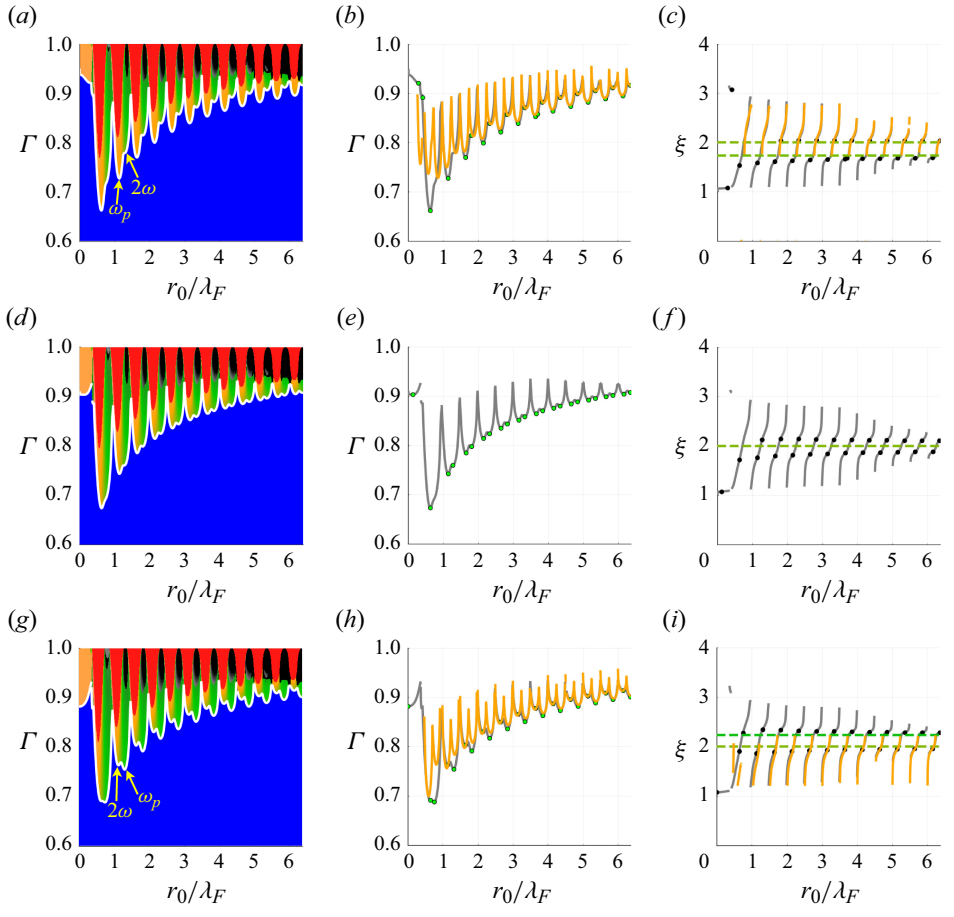

Figure 5. Orbital stability for walkers in convex potentials ($n > 0$) for the experimental parameters specified in § 3. The force power, n, increases with successive rows, assuming values (*a*)–(*c*) $n = 2$, (*d*)–(*f*) $n = 3$, and (*g*)–(*i*) $n = 4$. (*a*,*d*,*g*) Orbital stability diagrams, with the stability of circular orbits indicated using the same colour scheme as in figure 3. (*b*,*e*,*h*) Critical memory of instability. Numerically computed stability boundaries (grey curves) may be compared with the asymptotic solutions (orange curves) defined in (4.2*a*) and (4.4*a*). Green dots represent the critical radii of instability, for which instabilities arise at lowest memory. (*c*,*f*,*i*) Dependence of the wobble number, $\xi = S/\omega$, on the orbital radius along the stability boundary, as predicted by numerics (grey curves) and asymptotics (orange curves; see (4.2*b*) and (4.4*b*)). The black dots, which correspond to the critical radii of instability (green dots in panels *b*,*e*,*h*), lie close to the wobbling frequencies 2ω and $\omega_p = \sqrt{n+1}\omega$ (dashed horizontal lines). The wobble number (grey curves), increases monotonically with the orbital radius, r_0, then jumps downwards discontinuously at half-integer multiples of the Faraday wavelength.

to that of a Coriolis force, for which $\boldsymbol{F}\cdot\boldsymbol{n} = 2m\Omega r_0\omega \approx -2m|\Omega|u_0$ for inertial orbits. Indeed, the stability boundary for the conical potential is indistinguishable from that of the Coriolis force for $r_0/\lambda_F \gtrsim 0.5$ (see figure 6), with equivalent asymptotic stability boundaries (as may be seen by comparing (4.1*a*) and (4.1*b*) respectively to (4.2*a*) with $N = 0$ and $N = 1$). Nevertheless, there are two main differences. First, small-radius orbits ($r_0/\lambda_F \lesssim 0.25$) are unstable for a conical potential (see Appendix E), yet are stable for a Coriolis force (Oza 2014). Second, the $O(1/k_F r_0)$ detuning from resonant 2-wobbles persists for a conical potential (see 4.2*b*), but not for the Coriolis force (see 4.1*c*). Finally, we note that potential-driven wobbling with frequency $\omega_p = \omega$ is suppressed in the conical potential.

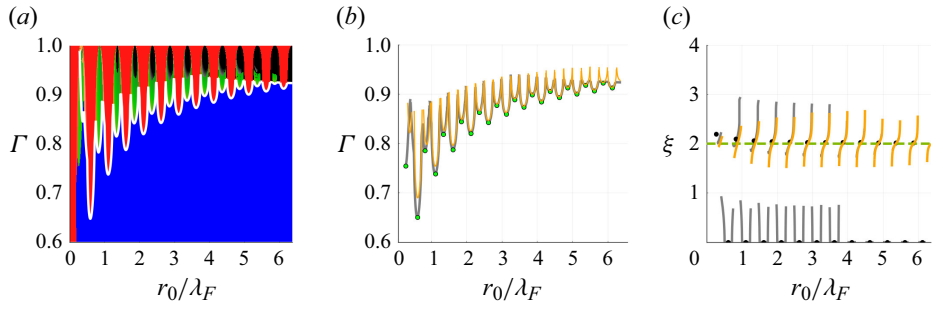

Figure 6. Orbital stability for walkers in a conical potential, equivalently a radially uniform central force, $\boldsymbol{F} = -k\boldsymbol{x}_p/|\boldsymbol{x}_p|$, for the experimental parameters specified in § 3. (*a*) Stability diagram, with the same colour scheme as in figure 3. The white curve denotes the stability boundary for the Coriolis system (see figure 3*c*). The strong agreement between the instability boundaries in the two systems is a consequence of the constancy of the Coriolis force for constant-speed motion. (*b*) Comparison between the numerically computed stability boundary (grey curve) and the asymptotic solutions (orange curves) defined using (4.2*a*). (*c*) Numerically computed (grey) and analytic solutions (orange, see 4.2*b*) for the wobble number, $\xi = S/\omega$, along the stability boundary, for $\xi < 4$. The black dots denote the critical memory of instability, corresponding to the green dots in (*b*).

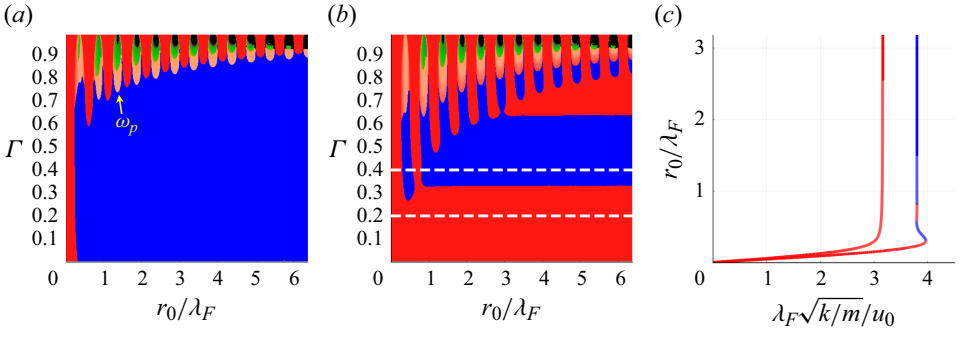

Figure 7. Orbital stability for walkers in concave potentials ($V(r) \propto r^{n+1}$ for $-1 < n < 0$ or $V(r) \propto \ln r$ for $n = -1$) for the experimental parameters specified in § 3, with the same colour scheme as in figure 3. (*a*) Stability diagram for $n = -0.5$. The potential-driven instability (light red) arises at a lower memory than the 2ω-wobbles (green); see table 3. (*b*) Stability diagram for a logarithmic potential. Monotonic instabilities represent the dominant instability mechanism, as the potential-driven instability occurs at a frequency $\omega_p = \sqrt{n+1}\omega = 0$ for $n = -1$. (*c*) Dependence of the orbital radius on the central force constant, k, for $n = -1$, with $\Gamma = 0.2$ and $\Gamma = 0.4$ corresponding to the dashed lines in panel (*b*). We note that portions of the orbital solution curve with positive slope are unstable with monotonically growing perturbations, in accordance with Theorem 1.

4.3.6. *Concave potentials*

For concave potentials with power-law form $V(r) \propto r^{n+1}$ for $-1 < n < 0$, perturbations either grow monotonically or are ω_p-wobbles (see figure 7*a*), in agreement with our asymptotic predictions (see table 3). However, for the logarithmic potential, $V(r) \propto \ln(r)$ (corresponding to $n = -1$), there is a qualitative change in the structure of the stability diagram in figure 7(*b*). Specifically, monotonic instabilities dominate (in accordance with $\omega_p = 0$), plateaus in the stability boundary emerge at $\Gamma \approx 0.35$ and $\Gamma \approx 0.65$ (associated with changes in slope of the orbital solution curve; see figure 7*c*), and the monotonic instability tongues resemble tear drops, which widen and merge at larger radius, resulting in islands of stability at high memory. As memory is further increased, these stability islands are terminated by an oscillatory instability, whose frequency is neither

commensurate with the orbital frequency nor equal to the potential-driven instability frequency, $\omega_p = 0$ (Tambasco *et al.* 2016). As these anomalous features violate the scaling of $\beta = O(\ln \hat{r}_0)$ leveraged in Appendix D, a new asymptotic framework to capture them will be left for future work. In particular, the tear-drop-shaped instability boundaries cannot be uniquely defined in terms of the orbital radius, thus precluding the development of explicit formulae for the critical memory.

5. Discussion

Orbital pilot-wave dynamics has provided one of the central paradigms for the emergence of quantisation and quantum-like statistics from classical pilot-wave dynamics (Bush & Oza 2020). The particle is able to access only a discrete number of orbitals owing to the dynamic constraint imposed on it by its quasi-monochromatic pilot-wave field (Fort *et al.* 2010). At high memory, the droplet switches intermittently between unstable periodic orbits (Harris & Bush 2014; Perrard *et al.* 2014*a*,*b*; Oza *et al.* 2014*b*). This physical picture suggests that the superposition of statistical states in quantum systems may be rooted in an underlying, but currently unresolved, chaotic pilot-wave dynamics, a perspective forwarded by Gutzwiller in his periodic orbit theory (Müller *et al.* 2005). Our analysis of orbital stability provides a step towards assessing the relative propensity of different orbital states in chaotic pilot-wave dynamics.

For droplets executing inertial orbits in a rotating frame, the onset of instability arises from a resonance between the orbital frequency, ω, and the destabilisation frequency, S, and is characterised by either monotonically growing perturbations ($S = 0$) or 2-wobbles ($S = 2\omega$). For droplets executing circular orbits under the influence of an axisymmetric potential, we have demonstrated that the natural frequency of radial oscillation is ω_p (see (2.5)), resulting in potential-driven instabilities at frequency $S = \omega_p$, in addition to monotonic and 2ω-instabilities. The difference between ω_p and its analogue in classical orbital mechanics (ω_c, see (2.3)) arises because the system acts to conserve orbital speed rather than angular momentum. Equation (2.5) indicates that in radial potentials, $V(r) \propto r^q$, for which $\omega_p = \sqrt{q}\omega$, stable circular orbits can arise in our system only if $q > 0$. In this case, the near-critical oscillatory modes of frequency ω_p are resonant if and only if q is a perfect square.

To characterise the emergence of wave-driven and potential-driven instabilities in different settings, we generalised our analysis to consider the confinement of a walking droplet by a power-law central force of the form $\boldsymbol{F} = -k|\boldsymbol{x}_p|^{n-1}\boldsymbol{x}_p$ with $n \geqslant -1$, for which $\omega_p = \omega\sqrt{n+1}$. When the central force increases with radial distance ($n > 0$), as is the case for a harmonic potential ($n = 1$), wave-driven and potential-driven wobbling instabilities are prevalent. The instability tongues in the stability diagram alternate between 2ω-wobbles and ω_p-wobbles every half wavelength with increasing orbital radius. Of particular interest is the case $n = 3$, for which the potential-driven instabilities are resonant with $\omega_p = 2\omega$, leading to merging pairs of 2ω and ω_p instability tongues. In this case, numerical simulations reveal that 2-wobbles are prevalent in the weakly unstable regime. When the spring force is radially uniform ($n = 0$), the stability diagram is similar in structure to that of the Coriolis force, consisting of alternating monotonic and 2ω-wobble instability tongues. Indeed, the asymptotic stability boundaries are precisely equal for the two systems. Finally, when the spring force decreases with radial distance ($-1 \leqslant n < 0$), monotonic instabilities are prevalent, particularly in the case of a logarithmic potential ($n = -1$), for which $\omega_p = 0$.

Our study also highlights the limitations of rationalising the onset of instability in terms of simple heuristic arguments (Labousse *et al.* 2016; Liu *et al.* 2023). Specifically, our

asymptotic and numerical investigations in § 4 demonstrated that the critical radii of the 2ω and ω_p instability tongues can alternate between being close to $\sin(2k_F r_0) = 1$ or $\sin(2k_F r_0) = -1$, depending on the power-law force, n (see table 3). As such, one cannot simply rationalise the critical radii at the onset of 2-wobbles in terms of the zeros of Bessel functions (Labousse *et al.* 2016), the minima of the wave energy (Liu *et al.* 2023), or the curvature of the mean wave field (Liu *et al.* 2023), all of which are independent of the confining force. Likewise, these heuristic arguments can neither distinguish between 2ω and ω_p wobbling instabilities, nor assess their relative likelihood as a function of memory. Instead, we find that the relative ordering of the 2ω and ω_p instability tongues is related to the observation that the wobble number, $\xi = S/\omega$, increases monotonically across pairs of wobbling instability tongues, with downward jumps arising when the orbital radius is close to a half-integer multiple of the Faraday wavelength (see figure 5). Rationalising this observation remains the subject of ongoing investigation.

As part of our analysis, we have developed Theorem 1 (see Appendix B), which provides a simple diagnostic for the onset of monotonic instabilities in a central or Coriolis force in terms of the slope of the orbital solution curve (see figure 3*a*,*b* and figure 7*c*). Specifically, if the confining potential decays too rapidly in space to rein in outward perturbations, then the perturbations grow monotonically in time and the circular orbit destabilises. Consequently, monotonic instabilities are more prevalent in concave potentials than convex potentials (see § 4). We have also used this result to justify the instability of small circular orbits for sub-linear central forces (see Appendix E). We note that this result is an extension of Theorem 1 of Oza *et al.* (2014*a*) for orbital pilot-wave dynamics in a Coriolis force. However, our proof does not rely explicitly on the particular properties of the stroboscopic pilot-wave system, and so may be applied more generally, to any classical particle orbiting in an axisymmetric potential or a Coriolis force field.

It is also worth considering the stability of walkers in an oscillatory potential of the form $V(r) \propto \mathrm{J}_0(k_F r)$, as was explored experimentally and numerically by Tambasco & Bush (2018). By using Bessel's equation to evaluate $V''(r_0)$ in (2.5), we compute $\omega_p = \omega\sqrt{r_0 k_F \mathrm{J}_0(k_F r_0)/\mathrm{J}_1(k_F r_0)}$, which corresponds to potential-driven wobbling when the argument of the square root is positive, and monotonic growth otherwise. When the orbital radius is such that $\mathrm{J}_0(k_F r_0)$ and $\mathrm{J}_1(k_F r_0)$ are of the same sign, radial perturbations oscillate in time, with the oscillation frequency increasing with proximity to the zeros of $\mathrm{J}_1(k_F r_0)$. However, when the signs of $\mathrm{J}_0(k_F r_0)$ and $\mathrm{J}_1(k_F r_0)$ differ, radial perturbations grow exponentially in time, giving rise to instability. Our theoretical treatment of walkers as constant-speed particles (see § 2.2) thus predicts that circular orbits are stable only within narrow radial intervals separated approximately by half the Faraday wavelength, in accordance with the experimental observations of Tambasco & Bush (2018). Such a case is particularly interesting given that the mean pilot wave of a droplet executing a circular orbit takes a comparable form in the high-memory limit (Tambasco & Bush 2018), so one can then consider the stability of an orbiting droplet in its self-potential.

Finally, our analysis has considered a single point in parameter space in the generalised pilot-wave framework (Durey & Bush 2021), corresponding to the experimental parameters used by Harris & Bush (2014). For example, in § 4.3, we have assumed that the dimensionless mass number satisfies $4M > 1$, as is the case in the laboratory. Our theoretical formalism allows for a broader exploration of orbital pilot-wave dynamics at a much wider range of parameter values, which will be the subject of future work. Of particular interest will be the small M, long-memory limit, where quantum effects are known to be most prevalent (Oza *et al.* 2018). In this long-memory limit, the instantaneous pilot-wave form converges to the mean (Durey, Milewski & Bush 2018), so one expects the self-potential associated with the mean pilot-wave form to play a role equivalent to

the applied potential in the orbital stability. This physical picture, which evokes the role of the quantum potential in Bohmian mechanics (Holland 1995), will be explored in an upcoming manuscript.

Funding. J.B. gratefully acknowledges the generous financial support of the NSF through grant CMMI-2154151 and the Office of Naval Research through grant N000014-24-1-2232.

Declaration of interests. The authors report no conflict of interest.

Author contributions. J.B. and M.D. conceived the project. N.L. was responsible for the mathematical and numerical developments, which were overseen by M.D. All authors contributed to the writing.

Data availability statement. The data that support the findings of this study are available from the corresponding authors, M.D. and J.B., upon reasonable request.

Appendix A. Orbital stability at low orbital memory

The regime of low orbital memory, $M_e^O \ll 1$, in which the droplet's horizontal velocity evolves slowly relative to the memory time, T_M, emerges for relatively large orbits or weak vibrational forcing. In this weak-acceleration limit, one may substitute the approximation $\boldsymbol{x}_p(t) - \boldsymbol{x}_p(s) \approx (t-s)\dot{\boldsymbol{x}}_p(t) - (1/2)(t-s)^2\ddot{\boldsymbol{x}}_p(t)$ into the wave force integral term in (3.2) and evaluate the resulting integrals (Bush *et al.* 2014). The droplet's trajectory equation may thus be approximated by the local form

$$\frac{\mathrm{d}\boldsymbol{p}}{\mathrm{d}t} + D_w(|\dot{\boldsymbol{x}}_p|)\dot{\boldsymbol{x}}_p = \boldsymbol{F}, \tag{A1a}$$

where $\boldsymbol{p} = m\gamma_B(|\dot{\boldsymbol{x}}_p|)\dot{\boldsymbol{x}}_p$ is the droplet's effective momentum, expressed in terms of the wave-induced added mass, or 'hydrodynamic boost factor',

$$\gamma_B(|\dot{\boldsymbol{x}}_p|) = 1 + \frac{gAk_F^2T_M^3}{2T_F\left(1 + (k_FT_M|\dot{\boldsymbol{x}}_p|)^2\right)^{3/2}}. \tag{A1b}$$

The wave force also gives rise to a speed-dependent drag coefficient,

$$D_w(|\dot{\boldsymbol{x}}_p|) = D\left[1 - \frac{c^2}{|\dot{\boldsymbol{x}}_p|^2}\left(1 - \frac{1}{\sqrt{1 + (k_FT_M|\dot{\boldsymbol{x}}_p|)^2}}\right)\right], \tag{A1c}$$

that drives the droplet towards the steady walking speed, u_0 (Bush *et al.* 2014). Specifically, the walking speed satisfies $D_w(u_0) = 0$, with $D_w > 0$ if $|\dot{\boldsymbol{x}}_p| > u_0$ and $D_w < 0$ otherwise.

Following the analysis of Bush *et al.* (2014) for steady circular orbits with radius r_0 and frequency $\omega > 0$, the orbital speed, $U = r_0\omega$, is equal to the free-walking speed, u_0. The orbital radius satisfies $r_0V'(r_0) = p(u_0)u_0$ for orbiting in a potential with force $\boldsymbol{F} = -\boldsymbol{\nabla}V(|\boldsymbol{x}_p|)$, and is defined as $r_0 = p(u_0)/(2m|\Omega|)$ for orbiting in response to a Coriolis force, $\boldsymbol{F} = -2m\boldsymbol{\Omega} \times \dot{\boldsymbol{x}}_p$, where $p(u) = m\gamma_B(u)u$. The orbital stability may be determined by defining the droplet's position and velocity as

$$\boldsymbol{x}_p(t) = r(t)(\cos\theta(t), \sin\theta(t)) \quad \text{and} \quad \dot{\boldsymbol{x}}_p(t) = u(t)(-\sin\phi(t), \cos\phi(t)), \tag{A2}$$

respectively. For small perturbations, we express the radius and speed as $r(t) = r_0 + \epsilon r_1(t)$ and $u(t) = u_0 + \epsilon u_1(t)$, where $0 < \epsilon \ll 1$, and likewise perturb the polar angles θ and ϕ. We then substitute this perturbation ansatz into (A1*a*) and use Taylor expansions to derive linear equations for the perturbed variables. Eliminating the perturbed polar angles yields a pair of coupled evolution equations for the perturbed radius and speed, as summarised as follows.

A.1. *Walking in a rotating frame*

When the droplet motion is subjected to a Coriolis force, the radial and speed perturbations evolve according to

$$\ddot{r}_1 + \omega^2 r_1 = \omega\left(\frac{u_0 p'(u_0)}{p(u_0)}\right) u_1 \quad \text{and} \quad p'(u_0)\dot{u}_1 + u_0 D'_w(u_0) u_1 = 0. \tag{A3}$$

The eigenvalues $s_\pm = \pm \mathrm{i}\omega$ reflect the translational invariance of the orbit and $s_0 = -u_0 D'_w(u_0)/p'(u_0)$ corresponds to decaying speed perturbations when $p'(u_0) > 0$. Circular orbits in a rotating frame are thus stable at low orbital memory.

A.2. *Walking in a central force*

For a droplet confined to an axisymmetric potential, perturbations evolve according to

$$\ddot{r}_1 + \omega_p^2 r_1 = \omega\left(1 + \frac{u_0 p'(u_0)}{p(u_0)}\right) u_1 \quad \text{and} \quad p'(u_0)\dot{u}_1 + u_0 D'_w(u_0) u_1 = -\frac{p(u_0)}{r_0}\dot{r}_1, \tag{A4}$$

where the natural frequency of radial perturbation, $\omega_p = \omega\sqrt{1 + r_0 V''(r_0)/V'(r_0)}$, is identical to the potential-driven wobbling frequency derived in § 2.2 for constant-speed particles. In the large-radius limit, the eigenvalues of (A4) are $s_0 = -u_0 D'_w(u_0)/p'(u_0) + O(r_0^{-2})$ and

$$s_\pm = \pm \mathrm{i}\omega_p - \frac{u_0\big(p(u_0) + u_0 p'(u_0)\big)}{2r_0^2\big(u_0^2 D'_w(u_0)^2 + \omega_p^2 p'(u_0)^2\big)}\left(u_0 D'_w(u_0) \pm \mathrm{i}\omega_p p'(u_0)\right) + O\big(r_0^{-4}\big), \tag{A5}$$

where s_0 is related to the decay of speed perturbations (as in the case of a Coriolis force) and $s_\pm$ reflect the natural frequency of radial oscillations. As $p(u_0) + u_0 p'(u_0) > 0$ in the regime that walking droplets may be observed in the laboratory (Turton 2020), we conclude that the real part of $s_\pm$ is negative, albeit close to zero. Consequently, we deduce that $s_\pm$ form a pair of near-critical stable eigenvalues in the weak-acceleration limit. Finally, we note that as ω_p does not depend explicitly on the wave-induced added mass, γ_B, for a fixed orbital radius, our analysis incorporates the Rayleigh oscillator model (Labousse & Perrard 2014) as a special case, for which $\gamma_B = 1$ and $D_w(u) = D_0(u^2/u_0^2 - 1)$.

Appendix B. Orbital stability framework

To investigate the stability of circular orbits in the hydrodynamic pilot-wave system, we recast the trajectory equation (3.2) into polar coordinates, namely

$$\boldsymbol{x}_p(t) = r(t)(\cos\theta(t), \sin\theta(t)), \tag{B1}$$

and perturb the droplet motion from a circular orbit at time $t = 0$ (Oza *et al.* 2014*a*). The radial ($l = r$) and tangential ($l = \theta$) force balances thus take the form

$$f_l(r, \dot{r}, \ddot{r}, \dot{\theta}, \ddot{\theta}) + \zeta f_{ext,l}(r, \dot{r}, \dot{\theta}) + \int_{-\infty}^{t} w_l(r(t), r(s), \theta(t) - \theta(s), t - s)\,\mathrm{d}s = \epsilon C_l \delta(t), \tag{B2}$$

where

$$f_r(r, \dot{r}, \ddot{r}, \dot{\theta}, \ddot{\theta}) = m(\ddot{r} - r\dot{\theta}^2) + D\dot{r} \quad \text{and} \quad f_\theta(r, \dot{r}, \ddot{r}, \dot{\theta}, \ddot{\theta}) = m(2\dot{r}\dot{\theta} + r\ddot{\theta}) + Dr\dot{\theta} \tag{B3}$$

represent the sum of the inertial and drag forces. Furthermore,

$$w_l(r_t, r_s, \varphi, \tau) = -\frac{F}{T_F}\frac{\mathrm{J}_1\left(\sqrt{r_t^2 + r_s^2 - 2r_t r_s\cos\varphi}\right)}{\sqrt{r_t^2 + r_s^2 - 2r_t r_s\cos\varphi}} W_l(r_t, r_s, \varphi)\mathrm{e}^{-\tau/T_M} \quad \text{for } l \in \{r, \theta\} \tag{B4}$$

are the radial and tangential components of the memory kernel, defined in terms of the current, $r_t = r(t)$, and prior, $r_s = r(s)$, radial position, the change in polar angle, $\varphi = \theta(t) - \theta(s)$, and the change in time, $\tau = t - s$, where $W_r = r_t - r_s\cos\varphi$ and $W_\theta = r_s\sin\varphi$. Finally, the magnitude of the perturbation is governed by the small parameter $0 < \epsilon \ll 1$, with $C_r = c_r$ and $C_\theta = r_0 c_\theta$ appearing in (B2) being arbitrary constants.

The droplet also evolves in response to the radial and tangential components on the external force field. For a Coriolis force, $\boldsymbol{F} = -2m\boldsymbol{\Omega} \times \dot{\boldsymbol{x}}_p$, the external force parameter, ζ, in (B2) is equal to the rotation rate, Ω, and the radial and tangential force components are

$$f_{ext,r}(r, \dot{r}, \dot{\theta}) = -2mr\dot{\theta} \quad \text{and} \quad f_{ext,\theta}(r, \dot{r}, \dot{\theta}) = 2m\dot{r}. \tag{B5}$$

For an attractive central force of the form $\boldsymbol{F} = -kF(|\boldsymbol{x}_p|)\boldsymbol{x}_p$ with $F(r) > 0$, we set ζ equal to the spring constant, k. The radial and tangential force components are thus

$$f_{ext,r}(r, \dot{r}, \dot{\theta}) = F(r)r \quad \text{and} \quad f_{ext,\theta}(r, \dot{r}, \dot{\theta}) = 0. \tag{B6}$$

Notably, the tangential component of the external force, $f_{ext,\theta}$, vanishes for steady orbital motion in the presence of either a Coriolis force or a central force, which we leverage in our analysis below. Recasting the radial and tangential force balances in the form (B2) allows us to streamline algebra and highlight the key features of the stability framework. Our analysis encompasses the results of Oza *et al.* (2014*a*) and Labousse *et al.* (2016) for a droplet orbiting in response to a Coriolis or central force, respectively.

B.1. *Linear stability analysis*

To analyse the linear stability of circular orbits, we assume that the droplet executes a circular orbit of radius r_0 and angular frequency ω for all $t < 0$. Following Oza (2014) and Liu *et al.* (2023), we parametrise steady circular orbits in terms of their orbital radius. We express the corresponding angular frequency as $\omega = \omega_0(r_0)$, and the force coefficient required to sustain the circular orbit as $\zeta = \zeta_0(r_0)$. It follows that $\omega_0(r_0)$ and $\zeta_0(r_0)$ satisfy the force balance equations $F_r(r_0, \omega_0(r_0), \zeta_0(r_0)) = 0$ and $F_\theta(r_0, \omega_0(r_0)) = 0$ (see 3.3), where

$$F_r(r_0, \omega, \zeta) = f_r(r_0, 0, 0, \omega, 0) + \zeta f_{ext,r}(r_0, 0, \omega) + \int_0^\infty w_r(r_0, r_0, \omega t, t)\,\mathrm{d}t, \tag{B7a}$$

$$F_\theta(r_0, \omega) = f_\theta(r_0, 0, 0, \omega, 0) + \int_0^\infty w_\theta(r_0, r_0, \omega t, t)\,\mathrm{d}t. \tag{B7b}$$

We note that the independence of F_θ on the force parameter, ζ, is a direct consequence of a vanishing tangential force, $f_{ext,\theta}(r_0, 0, \omega) = 0$, for steady orbital motion in the presence of a Coriolis or central force. In addition, the first two arguments of w_r and w_θ are both evaluated at r_0 to reflect the fact that the past trajectory is the circular orbit.

To account for the influence of the infinitesimal forcing at $t = 0$ on the droplet motion for $t > 0$, we substitute the ansatz $r(t) = r_0 + \epsilon H(t) r_1(t)$ and $\theta(t) = \omega t + \epsilon H(t)\theta_1(t)$ into (B2), where r_1 and θ_1 are the perturbed radius and polar angle, and $H(t)$ denotes

the Heaviside function. As the droplet position is continuous for all time, we conclude that $r_1(0) = \theta_1(0) = 0$; however, the acceleration impulse gives rise to a jump in droplet velocity, yielding $(\partial f_r/\partial \ddot{r})\dot{r}_1(0^+) = c_r$ and $(\partial f_\theta/\partial \ddot{\theta})\dot{\theta}_1(0^+) = r_0 c_\theta$ (Oza *et al.* 2014*a*; Liu *et al.* 2023), where

$$\frac{\partial f_r}{\partial \ddot{r}} = m \quad \text{and} \quad \frac{\partial f_\theta}{\partial \ddot{\theta}} = m r_0 \tag{B8}$$

for steady orbital motion with radius r_0.

By denoting the Laplace transforms of $r_1(t)$ and $\theta_1(t)$ as $R(s) = \mathscr{L}[r_1](s)$ and $\Theta(s) = \mathscr{L}[\theta_1](s)$, respectively, the Laplace transforms of the linearised evolution equations yield

$$\begin{pmatrix} \mathscr{A}(s) & -\mathscr{B}(s) \\ \mathscr{C}(s) & \mathscr{D}(s) \end{pmatrix} \begin{pmatrix} R(s) \\ r_0\Theta(s) \end{pmatrix} = \begin{pmatrix} c_r \\ r_0 c_\theta \end{pmatrix}. \tag{B9}$$

The functions in (B9) are defined in terms of $\mathrm{f}_r = f_r + \zeta f_{ext,r}$ and $\mathrm{f}_\theta = f_\theta + \zeta f_{ext,\theta}$ by

$$\mathscr{A}(s) = \left[\frac{\partial \mathrm{f}_r}{\partial r} + s\frac{\partial \mathrm{f}_r}{\partial \dot{r}} + s^2\frac{\partial \mathrm{f}_r}{\partial \ddot{r}}\right]_O + \int_0^\infty \frac{\partial w_r}{\partial r_t}(r_0, r_0, \omega t, t)\,\mathrm{d}t + \mathscr{L}\left[\frac{\partial w_r}{\partial r_s}(r_0, r_0, \omega t, t)\right], \tag{B10a}$$

$$-r_0\mathscr{B}(s) = \left[s\frac{\partial \mathrm{f}_r}{\partial \dot{\theta}} + s^2\frac{\partial \mathrm{f}_r}{\partial \ddot{\theta}}\right]_O + \int_0^\infty \frac{\partial w_r}{\partial \varphi}(r_0, r_0, \omega t, t)\,\mathrm{d}t - \mathscr{L}\left[\frac{\partial w_r}{\partial \varphi}(r_0, r_0, \omega t, t)\right], \tag{B10b}$$

where $\mathscr{C}$ and $\mathscr{D}$ are defined the same as $\mathscr{A}$ and $-\mathscr{B}$, respectively, but with f_r replaced by f_θ and w_r replaced by w_θ. In (B10), the notation $[F]_O$ means that the function F is evaluated for a steady circular orbit, so $[f_r]_O = f_r(r_0, 0, 0, \omega, 0)$, for example. The stability coefficients in (B11) are equivalent to those detailed in (C1). Finally, the asymptotic growth rates, s, governing the perturbation evolution are the poles of (B9) and thus satisfy $\mathscr{F}(s) = 0$, where

$$\mathscr{F}(s) = \mathscr{A}(s)\mathscr{D}(s) + \mathscr{B}(s)\mathscr{C}(s). \tag{B11}$$

B.2. *Properties of the stability function*

We proceed to establish the behaviour of $\mathscr{F}(s)$ for small s, which we will use to prove Theorem 1. In particular, rotational invariance of the pilot-wave system renders $\mathscr{B}(0) = \mathscr{D}(0) = 0$ and, hence, $\mathscr{F}(0) = 0$. We thus conclude that

$$\mathscr{F}(s) = \mathscr{F}'(0)s + O(s^2) \tag{B12}$$

for sufficiently small s, where $\mathscr{F}'(0) = \mathscr{A}(0)\mathscr{D}'(0) + \mathscr{B}'(0)\mathscr{C}(0)$. In fact, the stability coefficients in this case are very closely related to the equilibrium force balances (B7), with

$$\mathscr{A}(0) = \left[\frac{\partial \mathrm{f}_r}{\partial r}\right]_O + \int_0^\infty \left[\frac{\partial w_r}{\partial r_t}(r_0, r_0, \omega t, t) + \frac{\partial w_r}{\partial r_s}(r_0, r_0, \omega t, t)\right]\mathrm{d}t = \frac{\partial F_r}{\partial r_0}, \tag{B13a}$$

$$-r_0\mathscr{B}'(0) = \left[\frac{\partial \mathrm{f}_r}{\partial \dot{\theta}}\right]_O + \int_0^\infty t\frac{\partial w_r}{\partial \varphi}(r_0, r_0, \omega t, t)\,\mathrm{d}t = \frac{\partial F_r}{\partial \omega}, \tag{B13b}$$

and likewise

$$\mathscr{C}(0) = \frac{\partial F_\theta}{\partial r_0} \quad \text{and} \quad r_0\mathscr{D}'(0) = \frac{\partial F_\theta}{\partial \omega}. \tag{B13c}$$

We may thus equivalently write

$$r_0\mathscr{F}'(0) = \frac{\partial F_r}{\partial r_0}\frac{\partial F_\theta}{\partial \omega} - \frac{\partial F_r}{\partial \omega}\frac{\partial F_\theta}{\partial r_0}, \tag{B14}$$

where all derivatives are understood to be evaluated for (r_0, ω, ζ).

The relationship (B13) can be simplified further so as to deduce a more explicit expression for $\mathscr{F}'(0)$. To do so, we differentiate the force balance equations $F_r(r_0, \omega_0(r_0), \zeta_0(r_0)) = 0$ and $F_\theta(r_0, \omega_0(r_0)) = 0$ (see B7) with respect to r_0, giving (Oza *et al.* 2014*a*)

$$\frac{\partial F_r}{\partial r_0} + \frac{\partial F_r}{\partial \omega}\frac{\mathrm{d}\omega_0}{\mathrm{d}r_0} + f_{ext,r}\frac{\mathrm{d}\zeta_0}{\mathrm{d}r_0} = 0, \quad \frac{\partial F_\theta}{\partial r_0} + \frac{\partial F_\theta}{\partial \omega}\frac{\mathrm{d}\omega_0}{\mathrm{d}r_0} = 0. \tag{B15a}$$

By eliminating $\mathrm{d}\omega_0/\mathrm{d}r_0$ from (B15), we find that

$$\left\{\frac{\partial F_r}{\partial r_0}\frac{\partial F_\theta}{\partial \omega} - \frac{\partial F_r}{\partial \omega}\frac{\partial F_\theta}{\partial r_0}\right\} + f_{ext,r}\frac{\mathrm{d}\zeta_0}{\mathrm{d}r_0}\frac{\partial F_\theta}{\partial \omega} = 0, \tag{B16}$$

where upon applying (B14) to the term in curly brackets immediately yields the relationship

$$r_0\mathscr{F}'(0) + f_{ext,r}\frac{\mathrm{d}\zeta_0}{\mathrm{d}r_0}\frac{\partial F_\theta}{\partial \omega} = 0. \tag{B17}$$

Finally, we simplify the triple product by noting that the third term may be replaced by $r_0\mathscr{D}'(0)$ using (B13*c*), giving

$$\mathscr{F}'(0) = -f_{ext,r}(r_0, 0, \omega)\frac{\mathrm{d}\zeta_0}{\mathrm{d}r_0}\mathscr{D}'(0). \tag{B18}$$

This algebraic form generalises a similar result obtained by Oza *et al.* (2014*a*), and will be leveraged in the proof of Theorem 1.

THEOREM 1. *Consider orbital solutions satisfying $F_r(r_0, \omega_0(r_0), \zeta_0(r_0)) = 0$ and $F_\theta(r_0, \omega_0(r_0)) = 0$ (as defined in B7), where the angular frequency, $\omega = \omega_0(r_0)$, and force coefficient, $\zeta = \zeta_0(r_0)$, are parametrised by the orbital radius, r_0. The orbital solution is unstable with a real and positive root of $\mathscr{F}(s)$ (as defined in B11) in each of the following cases: (i) $\omega\, d\Omega_0/dr_0 < 0$ for a Coriolis force, $\boldsymbol{F} = -2m\boldsymbol{\Omega} \times \dot{\boldsymbol{x}}_p$, where the force coefficient is the bath rotation rate, $\zeta = \Omega$; (ii) $dk_0/dr_0 > 0$ for an attractive central force, $\boldsymbol{F} = -kF(|\boldsymbol{x}_p|)\boldsymbol{x}_p$ with $F(r) > 0$, where the force coefficient is the spring stiffness, $\zeta = k$.*

Proof. The proof uses the intermediate value theorem to establish a sufficient condition for there to exist a real and positive root of the stability function $\mathscr{F}(s)$, which we then apply for the cases of Coriolis or central forces. As all Laplace transforms in (B10) decay to zero as $s \to \infty$, we first note that

$$\mathscr{F}(s) \sim c_\infty s^4 \quad \text{as } s \to \infty, \quad \text{where } c_\infty = \frac{1}{r_0}\left[\frac{\partial f_r}{\partial \ddot{r}}\frac{\partial f_\theta}{\partial \ddot{\theta}} - \frac{\partial f_r}{\partial \ddot{\theta}}\frac{\partial f_\theta}{\partial \ddot{r}}\right]_O = m^2 > 0, \tag{B19}$$

as may be evaluated using (B8) and $\partial f_r/\partial\ddot{\theta} = \partial f_\theta/\partial\ddot{r} = 0$ (see B3). There thus exists a real and positive root of $\mathscr{F}(s)$ if $\mathscr{F}'(0) < 0$ (see B12). From (B18), this condition is equivalent to

$$f_{ext,r}(r_0, 0, \omega)\frac{\mathrm{d}\zeta_0}{\mathrm{d}r_0} > 0, \tag{B20}$$

where we have used that $\mathscr{D}'(0) > 0$ for the stroboscopic model (see the proof in Appendix F). We proceed by evaluating $f_{ext,r}(r_0, 0, \omega)$ for Coriolis and central forces to establish sufficient conditions on the sign of $\mathrm{d}\zeta_0/\mathrm{d}r_0$, as follows.

For a Coriolis force, we recall that $\zeta_0 = \Omega_0$ and that $f_{ext,r}(r_0, 0, \omega) = -2mr_0\omega$ (see B5), the sign of which depends on ω. We thus deduce from (B20) that there exists a real and positive root of $\mathscr{F}(s)$ when $\omega\,\mathrm{d}\Omega_0/\mathrm{d}r_0 < 0$, which proves case (*i*).

For a central force, we recall that $\zeta_0 = k_0$ and that $f_{ext,r}(r_0, 0, \omega) = r_0 F(r_0) > 0$ (see B6). We thus deduce from (B20) that there exists a real and positive root of $\mathscr{F}(s)$ when $\mathrm{d}k_0/\mathrm{d}r_0 > 0$, which proves case (*ii*). □

Theorem 1 determines the onset of monotonically growing orbital instabilities without needing to consider the fully stability problem (B11). For a Coriolis force, the theorem statement is identical to Theorem 1 of Oza *et al.* (2014*a*), except we prove explicitly the bound $\mathscr{D}'(0) > 0$ in Appendix F, a result that had previously been only verified numerically (Oza 2014). Furthermore, Theorem 1 extends the work of Oza *et al.* (2014*a*) to orbiting in attractive central forces, sidestepping the details of the pilot-wave system. This relative generality suggests that Theorem 1 is a fundamental property of orbital stability across a wide class of Coriolis and central force systems. Our proof also applies to non-Bessel wave kernels (with the proviso that $\mathscr{D}'(0) > 0$), as are needed to model the exponential far-field decay of the bouncer wave field (Damiano *et al.* 2016; Tadrist *et al.* 2018; Turton *et al.* 2018).

The physical interpretation of Theorem 1 for a central force is as follows, with the interpretation for inertial orbits in a Coriolis force being similar. Specifically, we rationalise the onset of monotonic instabilities through consideration of a perturbation from a circular orbit of radius r_0 with fixed spring constant $k_* = k_0(r_0)$. The perturbation is assumed to grow slowly, with the perturbed trajectory remaining nearly circular for all time; thus, the force balance equations (3.3) may be used to characterise the perturbed orbit. In the following argument, we denote the droplet's instantaneous radial position by $r(t)$ and assume that $\mathrm{d}k_0/\mathrm{d}r_0 > 0$. For outward perturbations, the spring constant k_* will be less than that needed for steady orbital motion at radius $r(t)$, as $k_* < k_0(r)$ when $r(t) > r_0$. Likewise, the spring constant, k_*, will exceed that needed for steady orbital motion at radius $r(t)$ for inward perturbations, since $k_* > k_0(r)$ when $r(t) < r_0$. Consequently, outward perturbations lead to a net outward radial force and inward perturbations result in a net inward force, causing the droplet's radial position to increase or decrease monotonically in time upon perturbation.

Appendix C. Orbital stability for pilot-wave hydrodynamics

As outlined in Appendix B, the asymptotic growth rates, s, associated with a perturbation from a circular orbit of radius r_0 and angular frequency ω are precisely the roots of the stability function $\mathscr{F}(s) = \mathscr{A}(s)\mathscr{D}(s) + \mathscr{B}(s)\mathscr{C}(s)$, which is defined in terms of the coefficients

$$\mathscr{A}(s) = m(s^2 + (n-1)\omega^2) + D\left(s + \frac{1}{T_M}\right) + Fk_F\left[\mathcal{C}_0(s) + \mathcal{I}_1(s) - \frac{n+1}{k_F^2 r_0}\frac{\partial \mathcal{I}_0(0)}{\partial r_0} - 2\mathcal{I}_0(0)\right], \tag{C1a}$$

$$\mathscr{B}(s) = (2-\Delta)m\omega s + Fk_F\left[\left(s\Delta - \frac{1}{T_M}\right)\frac{1}{k_F^2 r_0 \omega}\frac{\partial \mathcal{I}_0(0)}{\partial r_0} - \mathcal{S}_0(s)\right], \tag{C1b}$$

$$\mathscr{C}(s) = (2-\Delta)m\omega s + 2D\omega + Fk_F\left[\left(s\Delta + \frac{1}{T_M}\right)\frac{1}{k_F^2 r_0 \omega}\frac{\partial \mathcal{I}_0(0)}{\partial r_0} - \mathcal{S}_0(s)\right], \quad \text{(C1}c\text{)}$$

$$\mathscr{D}(s) = ms^2 + D\left(s - \frac{1}{T_M}\right) + Fk_F\left[\mathcal{C}_0(s) - \mathcal{I}_1(s)\right]. \quad \text{(C1}d\text{)}$$

The indicator $\Delta \in \{0, 1\}$ determines the type of applied force, with $\Delta = 0$ for a power-law central force of the form $\boldsymbol{F} = -k|\boldsymbol{x}_p|^{n-1}\boldsymbol{x}_p$ and $\Delta = 1$ for a Coriolis force, $\boldsymbol{F} = -2m\boldsymbol{\Omega} \times \dot{\boldsymbol{x}}_p$. For a Coriolis force, we additionally set $n = 1$ in (C1). The stability coefficients are defined in terms of the following integrals (for all integers $m \geqslant 0$ and $T_M \mathrm{Re}(s) > -1$):

$$\mathcal{I}_m(s) = \frac{1}{2T_F}\int_0^\infty \mathrm{J}_{2m}\left(2k_F r_0 \sin\left(\frac{\omega t}{2}\right)\right)\mathrm{e}^{-\left(\frac{1}{T_M}+s\right)t}\,\mathrm{d}t, \quad \text{(C2}a\text{)}$$

$$\mathcal{C}_m(s) = \frac{1}{2T_F}\int_0^\infty \mathrm{J}_{2m}\left(2k_F r_0 \sin\left(\frac{\omega t}{2}\right)\right)\cos(\omega t)\mathrm{e}^{-\left(\frac{1}{T_M}+s\right)t}\,\mathrm{d}t \quad \text{(C2}b\text{)}$$

$$\text{and} \quad \mathcal{S}_m(s) = \frac{1}{2T_F}\int_0^\infty \mathrm{J}_{2m}\left(2k_F r_0 \sin\left(\frac{\omega t}{2}\right)\right)\sin(\omega t)\mathrm{e}^{-\left(\frac{1}{T_M}+s\right)t}\,\mathrm{d}t. \quad \text{(C2}c\text{)}$$

These integrals encode the effects of path memory on the response of the walking droplet to perturbations from a circular orbit. Finally, we use integration by parts to recast the tangential force balance (3.3*b*) (with $\boldsymbol{F}\cdot\boldsymbol{t} = 0$) in terms of the stability integral $\mathcal{I}_0$, giving

$$\frac{2T_F}{T_M}\mathcal{I}_0(0) = 1 - \frac{r_0^2\omega^2}{c^2}, \quad \text{(C3)}$$

where $c = \sqrt{F/DT_F k_F}$ is the maximum steady orbital speed (Liu *et al.* 2023).

In summary, the orbital stability problem requires solving $\mathscr{F}(s) = 0$ and (C3) for s and ω, respectively, for a given orbital radius, r_0 (Oza 2014; Oza *et al.* 2014*a*), and is defined in terms of the stability coefficients (C1) and integrals (C2). The stability coefficients depend explicitly on the form of the applied force, as indicated by $\Delta \in \{0, 1\}$ in (C1). The stability integrals (C2) may be evaluated analytically (Liu *et al.* 2023, Appendix B), either in terms of Bessel functions of complex order,

$$\mathcal{I}_m(s) = \frac{\pi}{2\omega T_F}\mathrm{J}_{m+\mathrm{i}\eta}(k_F r_0)\mathrm{J}_{m-\mathrm{i}\eta}(k_F r_0)\mathrm{csch}(\pi\eta), \quad \text{(C4}a\text{)}$$

or in terms of infinite sums,

$$\mathcal{I}_m(s) = \frac{\eta}{2\omega T_F}\sum_{n=-\infty}^{\infty}\frac{(-1)^n \mathrm{J}_{m+n}(k_F r_0)\mathrm{J}_{m-n}(k_F r_0)}{\eta^2 + n^2}, \quad \text{(C4}b\text{)}$$

with

$$\mathcal{C}_m(s) = \frac{1}{2}\left(\mathcal{I}_m(s+\mathrm{i}\omega) + \mathcal{I}_m(s-\mathrm{i}\omega)\right), \quad \mathcal{S}_m(s) = \frac{1}{2\mathrm{i}}\left(\mathcal{I}_m(s-\mathrm{i}\omega) - \mathcal{I}_m(s+\mathrm{i}\omega)\right) \quad \text{(C4}c\text{)}$$

and $\eta = (s + T_M^{-1})/\omega$. Finally, we note that the various combinations of stability integrals appearing in (C1) may be reduced to a more concise form (Liu *et al.* 2023, Appendix B).

The orbital solution is unstable if there are any roots, s, of $\mathscr{F}$ satisfying $\mathrm{Re}(s) > 0$. By denoting s_* as the unstable root with largest real part, the instability is monotonic if $\mathrm{Im}(s_*) = 0$ and oscillatory otherwise. The stability function, $\mathscr{F}$, has a trivial eigenvalue at 0, corresponding to rotational invariance of the orbital motion. In the case of the Coriolis force, $\mathscr{F}$ has additional trivial eigenvalues at $\pm\mathrm{i}\omega$ due to translational invariance

(Oza *et al.* 2014*a*). It follows that the non-trivial roots of the stability problem satisfy $\mathscr{G}(s) = 0$, where

$$\mathscr{G}_{Cor.}(s) = \frac{\mathscr{A}(s)\mathscr{D}(s) + \mathscr{B}(s)\mathscr{C}(s)}{s(s^2+\omega^2)} \quad \text{and} \quad \mathscr{G}_{spr.}(s) = \frac{\mathscr{A}(s)\mathscr{D}(s) + \mathscr{B}(s)\mathscr{C}(s)}{s}. \tag{C5}$$

We apply the method of Delves & Lyness (1967) to find the roots of $\mathscr{G}$ in the domain over which $\mathscr{G}$ is analytic, i.e. $\mathrm{Re}(s)T_M > -1$. To ascertain whether a particular orbital state is stable or unstable, we typically use a rectangular integration contour spanning the domain $\mathrm{Re}(s) \in [0, 20]$ and $\mathrm{Im}(s) \in [0, 5]$, which we find to be sufficient for identifying all roots with a positive real part across the parameter regime outlined in § 3, and $0 \leqslant \Gamma \leqslant 0.999$.

Appendix D. The onset of orbital instability

To analyse the instability tongues, we recast the stability functions by evaluating all integrals analytically (Liu *et al.* 2023) and converting to dimensionless variables. Specifically, we take $T = 1/(ck_F)$ to be the unit of time, where $c = \sqrt{F/DT_F k_F}$ is the maximum steady orbital speed. Then, by defining $\hat{\mathscr{A}}(\hat{s}) = \mathscr{A}(s)T/D$ (and likewise $\hat{\mathscr{B}}$, $\hat{\mathscr{C}}$ and $\hat{\mathscr{D}}$) and introducing the dimensionless parameters $M = m/DT$ and $\zeta = T/T_M$, we obtain the tangential force balance

$$1 - \hat{r}_0^2\hat{\omega}^2 = \beta f_{00}(\beta, \hat{r}_0), \tag{D1a}$$

where $\hat{r}_0 = k_F r_0$, $\hat{\omega} = \omega T$ and

$$f_{ab}(\eta, \hat{r}_0) = \pi \,\mathrm{csch}(\pi\eta)\frac{\mathrm{d}^a}{\mathrm{d}\hat{r}_0^a}(\mathrm{J}_{-\mathrm{i}\eta}(\hat{r}_0))\frac{\mathrm{d}^b}{\mathrm{d}\hat{r}_0^b}(\mathrm{J}_{\mathrm{i}\eta}(\hat{r}_0)) \quad \text{for } a, b \in \{0, 1\}. \tag{D1b}$$

Furthermore, we define the stability function $\hat{\mathscr{F}}(\hat{s}) = \hat{\mathscr{A}}(\hat{s})\hat{\mathscr{D}}(\hat{s}) + \hat{\mathscr{B}}(\hat{s})\hat{\mathscr{C}}(\hat{s})$, where

$$\hat{\mathscr{A}}(\hat{s}) = M(\hat{s}^2 + \hat{\omega}^2(n-1)) + \frac{(n+1)}{\hat{r}_0\hat{\omega}}\left(\frac{\mathrm{i}}{\hat{r}_0} - f_{01}(\beta, \hat{r}_0)\right) + \frac{1}{\hat{\omega}}\left[f_{11}(\eta, \hat{r}_0) - f_{00}(\beta, \hat{r}_0)\left(1 + \frac{\beta\eta}{\hat{r}_0^2}\right)\right], \tag{D1c}$$

$$\hat{\mathscr{B}}(\hat{s}) = (2-\Delta)M\hat{\omega}\hat{s} - \frac{\mathrm{i}\hat{s}(\Delta+1)}{\hat{r}_0^2\hat{\omega}^2} + \frac{1}{\hat{r}_0\hat{\omega}}\left[\left(\frac{\hat{s}\Delta}{\hat{\omega}} - \beta\right)f_{01}(\beta, \hat{r}_0) + \eta f_{01}(\eta, \hat{r}_0)\right], \tag{D1d}$$

$$\hat{\mathscr{C}}(\hat{s}) = (2-\Delta)M\hat{\omega}\hat{s} + 2\hat{\omega} + \frac{\mathrm{i}\hat{s}(\Delta-1) - 2\mathrm{i}\hat{\omega}\beta}{\hat{r}_0^2\hat{\omega}^2} + \frac{1}{\hat{r}_0\hat{\omega}}\left[\left(\frac{\hat{s}\Delta}{\hat{\omega}} + \beta\right)f_{01}(\beta, \hat{r}_0) + \eta f_{01}(\eta, \hat{r}_0)\right], \tag{D1e}$$

$$\hat{\mathscr{D}}(\hat{s}) = M\hat{s}^2 + 2\hat{s} + \frac{\eta}{\hat{r}_0^2\hat{\omega}}\left[\beta f_{00}(\beta, \hat{r}_0) - \eta f_{00}(\eta, \hat{r}_0)\right], \tag{D1f}$$

$\hat{s} = sT$ represents the dimensionless complex growth rate, $\eta = \hat{s}/\hat{\omega} + \beta$ and $\beta = \zeta/\hat{\omega}$. Notably, ζ has been eliminated from the stability coefficients by using the tangential force balance (D1*a*). We aim to determine the critical value of the reciprocal orbital memory parameter, β, at which the growth rate, $\hat{s}$, has vanishing real part, writing $\hat{s} = \mathrm{i}\xi\hat{\omega}$ for real

$\xi = O(1)$. We recall that the Coriolis force corresponds to $\Delta = 1$ and $n = 1$; the central force corresponds to $\Delta = 0$ with n being the force power.

Our analysis hinges on applying asymptotic approximations to the functions $f_{ab}(\beta, \hat{r}_0)$. The argument of the Bessel function is $\hat{r}_0$ and the complex order is either $\pm \mathrm{i}\eta$, where $\eta = \beta + \mathrm{i}\xi$ along the stability boundary, or $\pm \mathrm{i}\beta$. Based on the assumed dominant balances $\beta = O(\ln \hat{r}_0) \ll \sqrt{\hat{r}_0}$ and $\xi = O(1)$, we conclude that the order of the Bessel function is much less than the argument, and thus apply large-argument expansions of Bessel functions (Abramowitz & Stegun 1948) to the stability problem (D1). The key difference to the Coriolis force problem (Liu *et al.* 2023) is that $\hat{\mathscr{D}}(\mathrm{i}\xi\hat{\omega}) = \mathrm{i}\xi\hat{\mathscr{C}}(\mathrm{i}\xi\hat{\omega}) + \mathrm{i}(\Delta - 1)M\hat{\omega}^2\xi + O(\hat{r}_0^{-3})$, and so terms that vanish for a Coriolis force ($\Delta = 1$) are significant for a central force ($\Delta = 0$). We thus require more terms in the expansion of the stability function for a central force. Upon using the tangential equation (D1*a*) to eliminate $\hat{\omega}$ and approximating $\mathrm{csch}(\pi\beta) = 2\mathrm{e}^{-\pi\beta} + O(\mathrm{e}^{-2\pi\beta})$ for large β, we find that the stability function takes the asymptotic form

$$\frac{(\hat{r}_0\hat{\omega})^2\hat{\mathscr{F}}(\mathrm{i}\xi\hat{\omega})}{\mathrm{i}\xi} = T_1 + T_3 + T_4 + O\left(\frac{\mathrm{e}^{-\pi\beta}}{\hat{r}_0^2}\right) + O\left(\frac{1}{\hat{r}_0^5}\right), \tag{D2}$$

where the successive terms, T_j, in the series expansion are

$$T_1 = \frac{\mathrm{e}^{-\pi\beta}}{\hat{r}_0}[-16(1 + \mathrm{e}^{-\mathrm{i}\pi\xi})\sin(2\hat{r}_0)], \quad T_3 = \frac{-4(1+2M)(-1+\Delta-n+\xi^2)}{\hat{r}_0^3},$$
$$T_4 = \frac{\mathrm{i}(-6\mathrm{i}\beta(1+4M)(-1+\Delta-n+\xi^2)+\xi(-3+\Delta(2-4M-16M^2)+\Delta^2(1+4M+4M^2)))}{\hat{r}_0^4}$$
$$- \frac{4\mathrm{i}M^2(3+n-\xi^2)+2(M+1)(\xi^2-n)}{\hat{r}_0^4}. \tag{D3}$$

Equation (D2) forms the foundation of our analysis of wave- and potential-driven instabilities, where it remains to find asymptotic solutions to β and ξ satisfying $\hat{\mathscr{F}}(\mathrm{i}\xi\hat{\omega}) = 0$ for $\hat{r}_0 \gg 1$.

To proceed, we identify dominant balances between $\mathrm{e}^{-\pi\beta}$ and powers of $\hat{r}_0$, for which there are two possibilities. If $-1 + \Delta - n + \xi^2 \neq 0$, then $T_3 \neq 0$ and the dominant balance is between terms T_1 and T_3. Otherwise, $T_3 = 0$ and so the dominant balance is between terms T_1 and T_4. In the presence of a Coriolis force, for which $\Delta = n = 1$, we note that $T_3 = 0$ only if $\xi^2 = 1$, which is a trivial eigenvalue corresponding to translational invariance. Thus, for non-trivial eigenvalues, the dominant balance for the Coriolis force system is only ever between terms T_1 and T_3, leading to resonant wave-driven instabilities (Liu *et al.* 2023). In contrast, both forms of dominant balance are possible for a central force ($\Delta = 0$), leading to both wave-driven ($T_3 \neq 0$) and potential-driven ($T_3 = 0$) instabilities.

When $T_3 \neq 0$, the dominant balance between T_1 and T_3 takes the form

$$-\frac{16\mathrm{e}^{-\pi\beta}(1+\mathrm{e}^{-\mathrm{i}\pi\xi})\sin(2\hat{r}_0)}{\hat{r}_0} - \frac{4(1+2M)(-1+\Delta-n+\xi^2)}{\hat{r}_0^3} = O\left(\frac{\mathrm{e}^{-\pi\beta}}{\hat{r}_0^2}\right) + O\left(\frac{1}{\hat{r}_0^4}\right), \tag{D4}$$

which we solve for β and ξ to leading order. Balancing the imaginary parts requires ξ to be an integer (to leading order), corresponding to resonant wave-driven instabilities. Balancing the real parts requires that integer to be even. The resulting asymptotic solutions

for β and ξ are detailed in (4.1) for a Coriolis force ($\Delta = n = 1$) and (4.2) for a central force ($\Delta = 0$).

Potential-driven wobbling instabilities emerge in a central force ($\Delta = 0$) when $T_3 = 0$, corresponding to the leading-order condition $n = \xi^2 - 1$, or $\xi = \sqrt{n+1}$. In this case, the dominant balance between terms T_1 and T_4 leads to

$$-\frac{16\mathrm{e}^{-\pi\beta}(1+\mathrm{e}^{-\mathrm{i}\pi\xi})\sin(2\hat{r}_0)}{\hat{r}_0} + \frac{\mathrm{i}\xi(4M-1)(2M+1)}{\hat{r}_0^4} = O\left(\frac{\mathrm{e}^{-\pi\beta}}{\hat{r}_0^2}\right) + O\left(\frac{1}{\hat{r}_0^5}\right). \quad \text{(D5)}$$

Provided that $\xi = \sqrt{n+1}$ is not an integer, we may use the dominant balance of the imaginary parts to solve for β to leading order, which gives rise to the potential-driven wobbling instability boundary detailed in (4.4). When $\xi = \sqrt{n+1}$ is an integer, potential-driven instabilities are resonant and a more sophisticated asymptotic treatment is necessary.

Appendix E. Instability of small orbits in a sub-linear central force

We proceed to show that $\mathrm{d}k_0/\mathrm{d}r_0 > 0$ for small-radius orbital solutions when $n < 1$. We then use Theorem 1 to conclude that these orbits are unstable to monotonically growing perturbations. For $k_F r_0 \ll 1$, the radial and tangential force balances (3.3) simplify to

$$-mr_0\omega^2 = \frac{Fk_F r_0\omega^2 T_M}{2T_F(\omega^2 + T_M^{-2})} - kr_0^n + O(r_0^3), \qquad D = \frac{Fk_F}{2T_F(\omega^2 + T_M^{-2})} + O(r_0^2), \quad \text{(E1)}$$

respectively. Along the orbital solution curve, $\omega = \omega_0(r_0)$ and $k = k_0(r_0)$ are thus

$$k_0(r_0) = r_0^{1-n}\omega_0^2(r_0)(m + DT_M) \quad \text{and} \quad \omega_0^2(r_0) = \frac{c^2k_F^2}{2} - \frac{1}{T_M^2}, \quad \text{(E2)}$$

where $c = \sqrt{F/DT_F k_F}$ is the maximum orbital speed. Notably, the orbital frequency, $\omega_0(r_0)$, for small circular orbits is the same as for a rotating frame (Oza *et al.* 2014*a*), and is valid provided that $T_M > T_W$, where $T_W = \sqrt{2}/ck_F$ is the memory time at the walking threshold (Durey *et al.* 2020*b*). As $\omega_0(r_0)$ is independent of r_0 to leading order, we deduce that

$$\frac{\mathrm{d}k_0}{\mathrm{d}r_0} = (1-n)r_0^{-n}(m + DT_M)\left(\frac{c^2k_F^2}{2} - \frac{1}{T_M^2}\right) \quad \text{for} \quad k_F r_0 \ll 1. \quad \text{(E3)}$$

We thus conclude that $\mathrm{d}k_0/\mathrm{d}r_0 > 0$ for sufficiently small orbital radii when $n < 1$ (with $T_M > T_W$), with orbits destabilising via monotonically growing perturbations.

Appendix F. Proof that $\mathscr{D}'(0) > 0$ for the stroboscopic model

To prove that $\mathscr{D}'(0) > 0$ for the stroboscopic pilot-wave model, with $\mathscr{D}(s)$ defined in (C1*d*), we first convert to dimensionless variables. As outlined in Appendix D, we define $\hat{\mathscr{D}}(\hat{s}) = \mathscr{D}(s)T/D$, where $\hat{s} = sT$ and $T = 1/(ck_F)$ is the unit of time. From (D1*e*), it thus remains to prove that $\hat{\mathscr{D}}'(0) > 0$, where

$$\hat{\mathscr{D}}'(0) = 2 - \frac{\pi\beta}{\hat{r}_0^2\hat{\omega}^2}\frac{\mathrm{d}}{\mathrm{d}\beta}\left(\beta\,\mathrm{csch}(\pi\beta)\mathrm{J}_{-\mathrm{i}\beta}(\hat{r}_0)\mathrm{J}_{\mathrm{i}\beta}(\hat{r}_0)\right). \quad \text{(F1)}$$

To proceed, we express the product in parentheses in (F1) in terms of an infinite sum, which is achieved by combining (C4*a*) and (C4*b*) with $m = 0$ to give

$$\pi\beta\,\mathrm{csch}(\pi\beta)\mathrm{J}_{-\mathrm{i}\beta}(\hat{r}_0)\mathrm{J}_{\mathrm{i}\beta}(\hat{r}_0) = \sum_{n=-\infty}^{\infty} \frac{\beta^2 \mathrm{J}_n^2(\hat{r}_0)}{n^2+\beta^2}. \tag{F2}$$

Substituting (F2) into (F1) and differentiating the sum term by term yields

$$\frac{\hat{r}_0^2\hat{\omega}^2}{2}\hat{\mathscr{D}}'(0) = \hat{r}_0^2\hat{\omega}^2 - \sum_{n=-\infty}^{\infty} \frac{n^2\beta^2 \mathrm{J}_n^2(\hat{r}_0)}{(\beta^2+n^2)^2}. \tag{F3}$$

We now recognise that the left-hand side of (F2) is the same as the right-hand side of the tangential force balance (D1*a*). We may thus express the tangential force balance in terms of the infinite sum in (F2) and then eliminate $\hat{r}_0^2\hat{\omega}^2$ from the right-hand side of (F3). A short calculation gives rise to the expression

$$\frac{\hat{r}_0^2\hat{\omega}^2}{2}\hat{\mathscr{D}}'(0) = 1 - \sum_{n=-\infty}^{\infty} \frac{\mathrm{J}_n^2(\hat{r}_0)\beta^2}{(\beta^2+n^2)}\left(1+\frac{n^2}{\beta^2+n^2}\right) = \sum_{n=-\infty}^{\infty} \frac{n^4 \mathrm{J}_n^2(\hat{r}_0)}{(\beta^2+n^2)^2}, \tag{F4}$$

where the right-hand side has been simplified using the identity $\sum_{n=-\infty}^{\infty} \mathrm{J}_n^2(\hat{r}_0) = 1$. As all terms in the final sum in (F4) are either zero or positive, we conclude that $\hat{\mathscr{D}}'(0) > 0$, and thus $\mathscr{D}'(0) > 0$ for the stroboscopic pilot-wave model.

References

Abramowitz, M. & Stegun, I.A. 1948 *Handbook of Mathematical Functions with Formulas, Graphs, and Mathematical Tables*, vol. 55, US Government printing office.

Bacot, V., Perrard, S., Labousse, M., Couder, Y. & Fort, E. 2019 Multistable free states of an active particle from a coherent memory dynamics. *Phys. Rev. Lett.* **122** (10), 104303.

Benjamin, T.B. & Ursell, F. 1954 The stability of the plane free surface of a liquid in vertical periodic motion. *Proc. R. Soc. Lond. A Math. Phys. Sci.* **225** (1163), 505–515.

Blitstein, A.M., Rosales, R.R. & Sáenz, P.J. 2024 Minimal quantization model in pilot-wave hydrodynamics. *Phys. Rev. Lett.* **132** (10), 104003.

Bush, J.W.M. 2015 Pilot-wave hydrodynamics. *Annu. Rev. Fluid Mech.* **47** (1), 269–292.

Bush, J.W.M. & Oza, A.U. 2020 Hydrodynamic quantum analogs. *Rep. Prog. Phys.* **84** (1), 017001.

Bush, J.W.M., Oza, A.U. & Moláček, J. 2014 The wave-induced added mass of walking droplets. *J. Fluid Mech.* **755**, R7.

Couder, Y., Protière, S., Fort, E. & Boudaoud, A. 2005 Walking and orbiting droplets. *Nature* **437** (7056), 208.

Cristea-Platon, T., Sáenz, P.J. & Bush, J.W.M. 2018 Walking droplets in a circular corral: quantisation and chaos. *Chaos* **28** (9), 096116.

Damiano, A.P., Brun, P.-T., Harris, D.M., Galeano-Rios, C.A. & Bush, J.W.M. 2016 Surface topography measurements of the bouncing droplet experiment. *Exp. Fluids* **57**, 163.

Delves, L.M. & Lyness, J.N. 1967 A numerical method for locating the zeros of an analytic function. *Maths Comput.* **21** (100), 543–560.

Durey, M. 2018 Faraday wave-droplet dynamics: a hydrodynamic quantum analogue. PhD thesis, University of Bath.

Durey, M. & Bush, J.W.M. 2021 Classical pilot-wave dynamics: the free particle. *Chaos* **31** (033136), 1–11.

Durey, M. & Milewski, P.A. 2017 Faraday wave-droplet dynamics: discrete-time analysis. *J. Fluid Mech.* **821**, 296–329.

Durey, M., Milewski, P.A. & Bush, J.W.M. 2018 Dynamics, emergent statistics and the mean-pilot-wave potential of walking droplets. *Chaos* **28** (9), 096108.

Durey, M., Milewski, P.A. & Wang, Z. 2020*a* Faraday pilot-wave dynamics in a circular corral. *J. Fluid Mech.* **891**, A3.

Durey, M., Turton, S.E. & Bush, J.W.M. 2020*b* Speed oscillations in classical pilot-wave dynamics. *Proc. R. Soc. Lond. A Math. Phys. Engng Sci.* **476** (2239), 20190884.

EDDI, A., SULTAN, E., MOUKHTAR, J., FORT, E., ROSSI, M. & COUDER, Y. 2011 Information stored in Faraday waves: the origin of a path memory. *J. Fluid Mech.* **674**, 433–463.

FORT, E., EDDI, A., MOUKHTAR, J., BOUDAOUD, A. & COUDER, Y. 2010 Path-memory induced quantization of classical orbits. *Proc. Natl Acad. Sci. USA* **107** (41), 17515–17520.

GOLDSTEIN, H., POOLE, C.P. & SAFKO, J.L. 2002 *Classical Mechanics*. Addison Wesley.

HARRIS, D.M. & BUSH, J.W.M. 2014 Drops walking in a rotating frame: from quantized orbits to multimodal statistics. *J. Fluid Mech.* **739**, 444–464.

HARRIS, D.M., MOUKHTAR, J., FORT, E., COUDER, Y. & BUSH, J.W.M. 2013 Wavelike statistics from pilot-wave dynamics in a circular corral. *Phys. Rev. E* **88** (1), 011001.

HÉLIAS, A. & LABOUSSE, M. 2023 Statistical self-organization of an assembly of interacting walking drops in a confining potential. *Eur. Phys. J. E* **46** (4), 29.

HOLLAND, P.R. 1995 *The Quantum Theory of Motion: an Account of the de Broglie-Bohm Causal Interpretation of Quantum Mechanics*. Cambridge University Press.

HUBERT, M., LABOUSSE, M., PERRARD, S., LABOUSSE, M., VANDEWALLE, N. & COUDER, Y. 2019 Tunable bimodal explorations of space from memory-driven deterministic dynamics. *Phys. Rev. E* **100** (3), 032201.

KURIANSKI, K.M., OZA, A.U. & BUSH, J.W.M. 2017 Simulations of pilot-wave dynamics in a simple harmonic potential. *Phys. Rev. Fluids* **2** (11), 113602.

LABOUSSE, M., OZA, A.U., PERRARD, S. & BUSH, J.W.M. 2016 Pilot-wave dynamics in a harmonic potential: quantization and stability of circular orbits. *Phys. Rev. E* **93** (3), 033122.

LABOUSSE, M. & PERRARD, S. 2014 Non-Hamiltonian features of a classical pilot-wave dynamics. *Phys. Rev. E* **90** (2), 022913.

LABOUSSE, M., PERRARD, S., COUDER, Y. & FORT, E. 2014 Build-up of macroscopic eigenstates in a memory-based constrained system. *New J. Phys.* **16** (11), 113027.

LIU, N., DUREY, M. & BUSH, J.W.M. 2023 Pilot-wave dynamics in a rotating frame: the onset of orbital instability. *J. Fluid Mech.* **973**, A4.

MOLÁČEK, J. & BUSH, J.W.M. 2013 Drops walking on a vibrating bath: towards a hydrodynamic pilot-wave theory. *J. Fluid Mech.* **727**, 612–647.

MÜLLER, S., HEUSLER, S., BRAUN, P., HAAKE, F. & ALTLAND, A. 2005 Periodic-orbit theory of universality in quantum chaos. *Phys. Rev. E* **72** (4), 046207.

OZA, A.U. 2014 A trajectory equation for walking droplets: hydrodynamic pilot-wave theory. PhD thesis, Massachusetts Institute of Technology.

OZA, A.U., HARRIS, D.M., ROSALES, R.R. & BUSH, J.W.M. 2014*a* Pilot-wave dynamics in a rotating frame: on the emergence of orbital quantization. *J. Fluid Mech.* **744**, 404–429.

OZA, A.U., ROSALES, R.R. & BUSH, J.W.M. 2013 A trajectory equation for walking droplets: hydrodynamic pilot-wave theory. *J. Fluid Mech.* **737**, 552–570.

OZA, A.U., ROSALES, R.R. & BUSH, J.W.M. 2018 Hydrodynamic spin states. *Chaos* **28** (9), 096106.

OZA, A.U., WIND-WILLASSEN, Ø., HARRIS, D.M., ROSALES, R.R. & BUSH, J.W.M. 2014*b* Pilot-wave hydrodynamics in a rotating frame: exotic orbits. *Phys. Fluids* **26** (8), 082101.

PERRARD, S., LABOUSSE, M., FORT, E. & COUDER, Y. 2014*a* Chaos driven by interfering memory. *Phys. Rev. Lett.* **113** (10), 104101.

PERRARD, S., LABOUSSE, M., MISKIN, M., FORT, E. & COUDER, Y. 2014*b* Self-organization into quantized eigenstates of a classical wave-driven particle. *Nat. Commun.* **5** (1), 3219.

PRIMKULOV, B.K., EVANS, D.J., BEEN, J.B. & BUSH, J.W.M. 2025*a* Nonresonant effects in pilot-wave hydrodynamics. *Phys. Rev. Fluids* **10** (1), 013601.

PRIMKULOV, B.K., EVANS, D.J., FRUMKIN, V., SÁENZ, P.J. & BUSH, J.W.M. 2025*b* Diffraction of walking drops by a standing Faraday wave. *Phys. Rev. Res.* **7** (1), 013226.

TADRIST, L., SHIM, J.-B., GILET, T. & SCHLAGHECK, P. 2018 Faraday instability and subthreshold Faraday waves: surface waves emitted by walkers. *J. Fluid Mech.* **848**, 906–945.

TAMBASCO, L.D. & BUSH, J.W.M. 2018 Exploring orbital dynamics and trapping with a generalized pilot-wave framework. *Chaos* **28** (9), 096115.

TAMBASCO, L.D., HARRIS, D.M., OZA, A.U., ROSALES, R.R. & BUSH, J.W.M. 2016 The onset of chaos in orbital pilot-wave dynamics. *Chaos* **26** (10), 103107.

TURTON, S.E. 2020 Theoretical modeling of pilot-wave hydrodynamics. *PhD thesis*, Massachusetts Institute of Technology.

TURTON, S.E., COUCHMAN, M.M.P. & BUSH, J.W.M. 2018 A review of the theoretical modeling of walking droplets: towards a generalized pilot-wave framework. *Chaos* **28** (9), 096111.